# The Effect of Cooling Rate on Structure and Properties of Closed-cell Aluminium Foams

M. Mukherjee[1,2,*], U. Ramamurty[3], F. Garcia-Moreno[1,2], J. Banhart[1,2]

[1]Helmholtz-Zentrum Berlin, Hahn-Meitner-Platz, 14109 Berlin, Germany

[2]Technische Universität Berlin, Hardenbergstrasse 36, 10623 Berlin, Germany

[3]Department of Materials Engineering, Indian Institute of Science, Bangalore 560012, India

**Abstract**

The application of different cooling rates as a strategy to enhance the structure of aluminium foams is studied. The potential to influence the level of morphological defects and cell size non-uniformities is investigated. AlSi6Cu4 alloy was foamed through the powder compact route and then solidified applying three different cooling rates. Foam development was monitored in-situ by means of X-ray radioscopy while foaming inside a closed mould. The macrostructure of the foams was analysed in terms of cell size distribution as determined by X-ray tomography. Compression tests were conducted to assess the mechanical performance of the foams and measured properties were correlated with structural features of the foams. Moreover, possible changes in the ductile-brittle nature of deformation with cooling rate were analysed by studying the initial stages of deformation. We observed improvements in the cell size distributions, reduction in micro-porosity and grain size at higher cooling rates, which in turn led to a notable enhancement in compressive strength.

*Keywords*: foams, cooling rate, microstructure, structure, mechanical property

---

* Corresponding author: M. Mukherjee. Phone: +49 30 8062 2820. Fax: +49 30 8062 3059. E-mail: manas.mukherjee@gmail.com

---

## 1. Introduction

Closed cell metal foams were initially envisioned as widely usable structural materials because of their expected high mass-specific strength and stiffness. Soon after their discovery it was realized that the strength of the foams is far below the values predicted by the scaling relations proposed by Gibson and Ashby that connect mechanical properties of the foam to the properties of the parent metal [1]. This discrepancy is widely considered to be caused by the presence of a non-uniform cell size distribution and macro- and meso-structural defects such as missing or broken cell walls, elliptical cells and curvature or wiggles in cell walls [2–6]. Since all these defects are believed to originate from manufacture of metal foams [4,7], it is of interest to modify the processing conditions in order to achieve a more uniform cell size distribution and to reduce morphological defects.

There are some approaches to improve the structure of aluminium foams produced through the powder compact foaming route in which $TiH_2$ is used as blowing agent. A heat-treatment of the $TiH_2$ is performed to shift the gas production towards a higher temperature [8]. This prevents the premature gas release that creates large cracks in the semi-solid state, which ultimately result in large cells in the final foam structure. Recently, hot compaction under vacuum has been demonstrated to produce foams with more regular cell size distribution than those produced through conventional compaction [9].

Since cooling rate influences the properties of aluminium alloys, one could expect that such effects are directly inherited to the corresponding foams. Micropores in the cell walls have a negative effect since they promote stress concentration and thereby crack generation [10,11]. A high cooling rate could possibly help in reducing the size of

such pores in the cell walls of the foams. Beside this, a higher cooling rate reduces grain size and thereby increases strength. Similar results could be expected for foams made from aluminium alloys. Moreover, the macrostructure could be influenced by the cooling rate as it determines the solidification time [12]. Finally, defects such as missing or broken cell walls can be reduced by increasing cooling rates [7].

The motivation of this work was to identify the effect of cooling rate on the micro and macrostructure of aluminium foams and the resulting mechanical properties. Closed-cell aluminium foams were prepared by the powder compaction route and three different cooling rates were applied to solidify the foams. Both micro and macrostructure of the foams were characterized by means of light microscopy and X-ray tomography. Strength changes were experimentally verified by compression tests. Moreover, the nature of deformation in the initial stages – ductile or brittle – was analysed after deformation to a low strain level.

## 2. Experimental

### *2.1 Foam preparation*

Foamable precursors of composition AlSi6Cu4 + 0.5 wt.% $TiH_2$ were prepared by powder processing from elemental powders of aluminium (Alpoco, purity 99.7%), silicon (Wacker Chemie, purity 99.5%), copper (Chempur, puritiy 99.5%) and the blowing agent titanium hydride (Chemetall, purity 98.8%). The $TiH_2$ was heat-treated at 480 °C for 180 minutes in air prior to its use. 20 g of powder of the above composition were mixed in a tumbling mixer for 15 minutes. The powder blend was subjected to uniaxial hot compaction with 300 MPa pressure for 300 s at 400 °C and tablets that are

36 mm in diameter and 7.3 mm thick were obtained. Cuboid samples with dimensions $28 \times 24 \times 7.3$ mm$^3$ were cut from each tablet and were then foamed.

Foaming was conducted inside a furnace that is partially transparent to X-rays and the entire process was monitored in-situ by means of X-ray radioscopy. A schematic of the foaming set-up is shown in Fig. 1. The mould was made of a 2 mm thick stainless steel tube of square cross-section with the open ends (in the X-ray direction) covered with stainless steel plates (total $2 \times 0.3$ mm thick) that were fastened together by stainless steel screws. Heating to 610 °C was performed by three 150 Watt halogen lamps equipped with an IR reflector. The temperature was measured at the lower surface of the sample by a thermocouple that was inserted from below through a hole in the steel tube. For every sample, foaming was stopped after the foam had completely filled the mould as seen in the X-ray projected images. Natural cooling as well as forced air cooling was employed to solidify the foams. The rate of cooling was varied by controlling the air flow of the pressurized air, which was directed towards the thin steel plates. Using indirect cooling prevents possible foam damage by the direct contact between the forced air and the fragile liquid foam. A total of three cooling rates were employed. The cooling rate was measured as the average cooling rate between the liquidus (605 °C) and solidus (525 °C) temperature of the alloy. The foams produced will be referred to as S, M and H after their cooling conditions: slowest (0.9 K/s), medium (2.5 K/s) and highest (3.5 K/s), respectively. Table 1 summarizes the 20 samples investigated.

*2.2. Structural and mechanical characterization*

One sample for each cooling rate was used for optical microscopy. The foam samples were embedded in cold-curing resin (Kulzer), mechanically ground using 120–4000 grit silicon carbide paper, polished successively with 3 and 1 μm diamond paste, and finally polished with a $SiO_2$ suspension on a smooth cloth. The rest of the samples from each cooling rate group were used for compression tests as indicated in Table 1. For these tests, the outer skins of the foams were removed, leading to final dimensions of 20 × 20 mm in cross-section and 18 mm in height, see Fig. 2. Prior to testing, X-ray tomography was performed on each sample using the same X-ray source as for radiography but in addition rotating the samples through 360° in steps of 1° while acquiring images after each step. Three-dimensional (3D) reconstruction of the data was performed using the commercial software Octopus. After reconstruction, the commercial software VGStudioMax 1.2.1 was used to extract 2D and 3D sections of the foam. The 2D cell size distribution of these samples was calculated by analyzing six reconstructed tomographic slices from each sample as shown in Fig. 2. This analysis was performed by using the software ImageJ 1.35j. For cell size analysis, only the cells larger than 0.1 $mm^2$ were considered.

Quasi-static compressions tests were carried out in a Zwick/Roell Z100 materials testing machine at a displacement rate of 1 mm/min up to nominal strains of 7, 25 and 70%, see Table 1. Additional X-ray tomography was performed on the samples that were strained up to 7 and 25%. Note that these two strains approximately correspond to that just at the beginning of the plastic deformation of the foams and to that in the steady-state plastic deformation regime (or the plateau in the stress-strain regime). After this, the microstructure of the samples with 7% strain was analyzed to ascertain the origins of plastic deformation in these foams.

## 3. Results

### *3.1. Foam characterization*

#### *3.1.1. Cell wall microstructure*

The microstructures from each cooling rate group are shown at two magnifications in Fig. 3. As cooling rate varies, the dendrite arm spacing (DAS) (or the grain size) and the size of cell wall porosity change significantly. While the DAS is 40–50 μm for S foams, it is 20 μm for H foams. The porosity in the cell walls can be classified as shrinkage or gas type. While the former is characterized by irregularly shaped pores, pores created by gas release are usually circular [13]. Large shrinkage and gas porosities are seen in the S foam, Fig. 3a and 3b. In the M and H foams, the size of both types of pores is significantly smaller. In fact, at low magnification, shrinkage porosities are hardly detectable in the M and H foams, see Fig. 3c and 3e, and are evenly distributed throughout the microstructure. Some of the shrinkage pores in the S foam were found to be connected with the main porosity (i.e., cell) of the foam; one such example is shown in Fig. 4. The size of the gas pores also decreases as cooling rate increases.

#### *3.1.2. Foam macrostructure*

The structure of the foams was analysed in terms of their 2D cell size distribution and cell circularity. Cell size is represented as an equivalent diameter $D$ of a circle with the same area. The circularity $C$ of a cell is defined as $4\pi A/P^2$ where $A$ and $P$ are the area and perimeter of that cell. If $C$ approaches 1, the cell resembles a circle. The results are presented in Figs. 5–7 and are summarized in Table 2. The errors given in

Table 2 and in the entire article represent standard deviation. For each cooling rate, the analysis was performed by taking account of all the cells from all the samples in that cooling rate group. Thus, the total number of cells analysed was 3126 (from 36 2D sections), 2933 (from 30 2D sections) and 3371 (from 36 2D sections) for S, M and H foams, respectively.

The mean circularity $C_{mean}$ of the cells was determined by calculating the arithmetic average. The mean cell diameter $D_{mean}$ was determined in three different ways. The first way was to calculate the arithmetic average of all cell diameters [14]. Another two ways were the cell size distributions based on number fraction [15] and area fraction [16] as shown in Figs. 5 and 6, respectively. *Area fraction*, which is the 2D counter part of *volume fraction*, is defined as the area contribution of a certain cell size class compared with the total area of all the cells. This can be given as

$$\text{Area fraction of cells with diameter } D_i = \frac{N_i \times \frac{1}{4}\pi D_i^2}{\sum_i N_i \times \frac{1}{4}\pi D_i^2} \times 100\%, \qquad (1)$$

where $N_i$ is the total number of cells with an equivalent diameter $D_i$. The distributions are fitted better by a log-normal distribution function than by a Gaussian distribution function (not shown). The goodness of the fittings is indicated by the $R^2$ values in Table 2. $D_{mean}$ as determined from each distribution is given in Table 2.

Large cells, being considerably compliant vis-à-vis small cells, are likely to undergo plastic collapse at lower loads. Consequently, the deformations of larger cells have a higher impact on the deformation behaviour of the foams. For this reason, when considering the mechanical behaviour of foams, the value for $D_{mean}$ determined from the distribution based on area fraction is more realistic than that determined by the other two methods. Table 2 shows that $D_{mean}$ determined from Fig. 6 (area fractions) is the

highest among all the three methods employed. Henceforth, we will use only those $D_{mean}$ values that were determined from Fig. 6. The H foams have the largest $D_{mean}$ whereas in the S and M foams $D_{mean}$ has the same value. The highest $R^2$ value (0.95) for the M foams in Table 2 suggests that the cells in these foams are more uniformly distributed than in the S and H foams.

Fig. 6 shows that in all the foams the larger cells have a significant amount of area fraction. In order to obtain a quantitative estimation of the amount of large cells, we use the following method: the cells with a $D$ larger than two standard deviations above $D_{mean}$ are considered as large cells. $D_{mean}$ is not the same in all the foams. Therefore, in order to compare the results from all the foams, we consider the lowest $D_{mean}$ and the respective standard deviation, i.e. of the S foams, in Table 2. The boundary between small and large cells is indicated in Fig. 7. The area and number fraction of the large cells are presented in Table 3. Both the area and the number fraction of large cells indicate that the S and H foams contain a greater amount of large cells than the M foams. We also studied the largest cells in each of the seventeen foams analysed. It was observed that the four largest cells in Fig. 7b (M foams) belong to a single sample, whereas the cells with similar or larger size in each of Figs. 7a (S foams) and 7c (H foams) belong to different samples.

$C_{mean}$ in all the foams is approximately the same, see Table 2. However, if $C$ of individual cells is considered, there is a noticeable difference in the circularity of the large cells. This can be seen in Fig. 7 where $C$ is shown as a function of $D$. The number of large cells with low $C$, say, less than 0.6, is higher in the H foams than the number of large cells with the same C in the M foams, see Figs. 7b and 7c.

*3.1.3. Density*

The density of the samples was determined by dividing their weight by their volume. Relative density, $\rho^*$, is defined as the ratio of the density of the foam to the density of the constituent dense solid. Although all the precursors were identical, $\rho^*$ varied among the differently cooled foams, M foams being the most dense as shown in Table 4.

*3.2. Mechanical properties*

*3.2.1. Compression behaviour*

Representative stress–strain curves obtained from foams of each cooling rate group are shown in Fig. 8. Data from all the samples are given in Table 4. The first peak value in the plastic part of the stress–strain curve was chosen as the plastic strength ($\sigma_p$). $\sigma_p$ is highest in the M foam, followed by that in the H and S foams. The energy absorbed by the foam per unit volume, $W$, is the area under the stress–strain curve up to densification and is estimated according to the following equation [17]:

$$W(\varepsilon_d) = \int_0^{\varepsilon_d} \sigma(\varepsilon) d\varepsilon \,, \qquad (2)$$

where $\varepsilon_d$ is the densification strain. The approach to evaluate $\varepsilon_d$ from a stress–strain curve is shown in Fig. 8. Two straight lines were drawn. The first one was the linear fit between strain 20 and 40% (between points 1 and 2) and the second one was the tangent to the stress–strain curve at 65% strain (point 3). The strain corresponding to the intersection of these two lines is taken as $\varepsilon_d$. The trend in $W$ is similar to that seen in $\sigma_p$. Note that the number of samples used for estimating $W$ is less than that for $\sigma_p$ since

deformation of some samples was stopped after 7 and 25% strains, less strain than $\varepsilon_d$, see Table 1.

Fig. 8 also shows the energy absorption efficiency, $\eta$, which is defined as [18,19]

$$\eta(\varepsilon) = \frac{\int_0^{\varepsilon} \sigma(\varepsilon) d\varepsilon}{\sigma_{\max}(\varepsilon)\varepsilon}, \quad (3)$$

where $\sigma_{\max}(\varepsilon)$ is the maximum stress experienced by the foam up to the strain $\varepsilon$. Ideal foams are those that exhibit a constant plateau stress in compression and hence $\eta = 1$ (or 100%) for them, whereas $\eta = 0.5$ for elastic-brittle solids [1]. The deviation from the ideal foam's response can be gauged by examining the energy absorption efficiency, $\eta$. Typically, $\eta$ reaches a value of ~90% within the first 10% $\varepsilon$ and remains constant up to a strain of ~60% in metallic foams. Note that this is the feature that makes these materials attractive candidates for impact energy absorption [18]. Fig. 8 suggests that $\eta(\varepsilon)$ is insensitive to the cooling rate, reaching a maximum of ~80% at 7–8% strain, exhibiting a plateau until ~40% strain and subsequently decreasing upon further straining. These features are broadly similar to those seen in commercial Al foams such as 'Alporas' [19].

*3.2.2. Deformation initiation*

Tomographs obtained from the samples that were deformed up to 7% strain are shown in Fig. 9, which make it clear that plastic deformation initiates by buckling of thin cell walls. Some of the deformed cell walls already show cracks at this stain level as seen in Fig. 9a. Some large cracks were visible in the tomographic reconstructions,

but the small cracks became visible only under the microscope. In all the foams, both buckling and cracking of the cell walls were observed. However, in the S foam most of the deformed cell walls developed cracks, whereas in the M and H foams relatively few cracks were observed in the deformed cell walls. Although some cell walls appeared to be free of cracks in the X-ray tomograms of the S foam, see square-marked part in Fig. 9a, their microstructure revealed cracks as can be seen in Fig. 10a. In contrast, at higher cooling rate, even heavily deformed cell walls did not show any cracks, see Fig. 10b. Fig. 10a reveals that a large crack has formed in a pre-existing about 100 µm pore within a cell wall.

Tomograms obtained at a more advanced stage of deformation (25% strain) in the S and H foams are shown in Fig. 11. Both foams show a similar crushing behaviour. A major amount of deformation was localized as crush bands, which is characteristic of deformation in Al foams [20–22]. In Fig. 11, the crush bands form an angle of about 60° with the loading axis. Inside the crush bands, both buckling and cracking of cell walls took place.

## 4. Discussion

### *4.1. Influence of cooling rate on density and macrostructure*

When foaming is performed inside a closed mould and the foaming time is set appropriately, a foam of reproducible volume – that of the mould – and density can be obtained. However, this does not ensure reproducible foam properties. A small change in the contact conditions between the mould surface and foamable precursor can change the heat transfer and consequently the initiation of foaming [23]. As a result, even for

seemingly identical foaming conditions, the effective foaming time can vary significantly from one foaming trial to another. If heating is continued after the foam has filled the mould, internal pressure can cause significant cell wall rupture. Since the moment of mould filling is not exactly known *a priori* in a closed mould, the foam structure can vary significantly. In the present study, the foaming process was monitored *in-situ* using X-ray radioscopy, see Fig. 1. In this way, reproducible foaming was achieved. The density variations among S, M and H foams were not caused by irreproducible foaming but are due to the differences in the cooling rate.

Gravity-driven drainage in liquid metal foams is a well-known phenomenon [24,25]. The more time a foam spends in the liquid state, the more drainage can induce a density profile along the height of the foam, the bottom part being of highest density [25]. Accordingly, the slowest cooling foams had a relatively denser bottom layer than the M and H foams due to a longer solidification time in the former. During removal of the surface skins, especially the bottom one, more solid material was removed from the S foams. This automatically makes the S foams lighter. One would expect that the H foams are the densest since the drainage for these foams is smallest due to fast solidification. But that is not the case as can be seen in Table 4, the reason of which is given in the following.

The density of foams increases with a decrease in cell size and increase in cell circularity [12,14,26]. This is due to an increase in the amount of material in the Plateau borders. In the H foams, both $D_{mean}$ and the amount of large cells are higher than the M foams as shown in Table 2 and Table 3. Moreover, the H foams contain more large cells with low circularity compared to the M foams. This reflects that the density of the H foams is less than of the M foams.

Another consequence of different solidification time is the variation in the extent to which cell wall rupture takes place. Drainage leads to thinning of cell walls. Below a certain cell wall thickness rupture is triggered. Consequently, the number of rupture events in the S foams should be the highest. A higher cooling rate increases the temperature gradient in the H foams. This, in turn, can increase the probability of cell wall rupture due to thermal shock [27]. Rupture leads to the coalescence of two cells into a larger one. Therefore, both the S and H foams contain more large cells than the M foams as shown in Table 3.

*4.2. Influence of cooling rate on microstructure*

At the higher cooling rate, the grain size (or DAS) is reduced mainly because of two reasons: firstly, the driving force for nucleation is increased due to a higher degree of undercooling; secondly, grain growth is limited due to a decrease in solidification time and a larger number of grains growing throughout the volume while hindering the growth of each other [28]. Therefore, the DAS changes significantly from S to M foams, whereas it does not vary significantly from M to H foams since the difference in the cooling rate is smaller here. Cooling rate is also known to influence the morphology of Si particles [29]. However, no such change was observed since the variation in cooling rate in the present study was insufficient.

Besides grain size, cooling rate also influences the size of both types of porosities. As shrinkage porosity is closely associated with grain size, a decrease in the latter immediately suggests a decrease of the former as can be observed in Fig. 3. Gas porosity is caused by the precipitation of dissolved hydrogen in a melt during solidification. At high cooling rates, a melt quickly gets saturated with hydrogen and as

a result, hydrogen porosity can nucleate at many places. However, because of the shorter time available for gas diffusion at a higher cooling rate, those pores do not grow significantly in size [30]. Consequently, the gas porosities are smaller in the M and H foams than in the S foams.

*4.3. Influence of cooling rate on mechanical properties*

The height of the sample ($h$ = 18 mm) is the smallest among all the three dimensions. $h/D_{mean}$ is at least 7 even considering the largest $D_{mean}$ value in Table 2. Even considering the boundary value ($D$ = 3.18 mm) between small and large cells, $h/D_{mean}$ is still more than 5. This is necessary to avoid size effects to obtain reliable compressive strengths [22,31]. Note that this criterion is only necessary when foams contain defects. For defect-free foams, even $h/D_{mean}$ = 2 is sufficient for reliable measurement [5]. No defects such as missing or broken cells were observed in the foams used in this study. This can also be confirmed from the tomograms shown in Figs. 9 and 12. This is due to the high cooling rates applied which prevent generation of such defects during solidification [7]. This further assures that the sample size used in this study was adequate for reliable measurements.

Compressive strength $\sigma_p$ and other mechanical properties of metal foams follow relations with its relative density $\rho^*$ [1,32] such as:

$$\sigma_p = F \cdot (\rho^*)^n , \quad (4)$$

where $F$ and $n$ are constants. Table 4 shows that both M and H foams have higher $\sigma_p$. However, whether this is a result of higher cooling rate in those samples or an artefact of an increased relative density needs to be examined. For this, $\sigma_p$ values were normalised by $(\rho^*)^n$. The most reported values of $n$ are in the range of 1.5–2 [1,19,32].

The normalised values of $\sigma_p$ for both $n$ = 1.5 and $n$ = 2 are listed in Table 4. Even after normalisation, the M foams exhibit the best strength, a reflection of its better overall quality as discussed below.

The mechanical properties of foams are determined both by their microstructural [10,11,33] and macrostructural [2,5] features. For a given amount of microstructural porosity, the specific porosity area per unit cross section decreases with the size of the individual pores. Thus, the load bearing capacity of the structure increases as the size of the pores decreases. Unlike gas pores that are mostly spherical, shrinkage pores could act as stress concentration points because of their irregular shape. Large shrinkage pores in the S foams may also act as pre-existing cracks such as the one shown in Fig. 4 and thereby lead to failure in an early stage of deformation. Therefore, from the microstructural point of view, it is expected that both the M and H foams possess a higher strength than the S foams.

Coming to the macrostructural features, the variation in $\sigma_p$ of the foams can also be understood by studying their cell size and circularity. As already mentioned, larger cells have an higher impact on the strength of the foams since deformation usually initiates at larger cells [20,34,35]. Therefore, $\sigma_p$ is mainly determined by the largest cells in foams. Table 3 shows that the number of large cells is less in the M foams than in the S and H foams. Moreover, the largest cells observed in the M foams are from only one out of five samples, whereas the cells with same $D$ in the S and H foams are from multiple samples. Consequently, the $\sigma_p$ of the M foams is the highest as shown in Table 4.

The large cells in the M foams have higher $C$ values than the large cells in the S and H foams as shown in Fig. 7. This implies that the cell walls associated with the

large cells in the M foams are relatively thicker than in the other two foams. Therefore under loading, the large cells in the S and H foams are more unstable than the large cells in the M foams [36].

As mentioned earlier, no significant difference between the microstructures of the M and H foams exists. Therefore, the difference in $\sigma_p$ in these foams is mainly attributed to their macrostructures. This is further demonstrated in Fig. 12. Both the foams shown there have the same density, but different macrostructures as visible in their tomographic sections and cell size distributions. Although $D_{mean}$ is identical in both foams, cells are more uniformly distributed in the M foam, see Figs. 12b and 12d. Considering the large cells for which $D > 3.18$ mm, the area and number fraction of the large cells in the M foam is 7% and 1%, respectively. For the H foam, they are 30% and 4%, respectively. Accordingly, the M foam shows higher strength vis-à-vis the H foam although both have similar densities.

The microstructure of the H foams is superior to that of the S foams as shown in Fig. 3. However, their macrostructure has mixed characteristics. The amount of large cells is slightly higher in the S foams, see Table 3. On the other hand, $D_{mean}$ is higher in the H foams as shown in Table 2. Therefore, it is not clear which of these two foams are better. In fact, the normalised $\sigma_p$ in Table 4 are identical for both the foams for coefficient $n = 2$. Nevertheless, there is no doubt that the M foams are the best among all the foams studied.

Like compressive strength, energy absorption also increases with cooling rate and has the highest value for M foams for the same reason responsible for the enhancement of $\sigma_p$ as described above. Interestingly, there is no difference in their energy absorption efficiencies as shown in Fig. 8.

*4.4. Ductile–brittle nature of deformation*

AlSi6Cu4 foams are mostly ductile in nature and the stress–strain responses of such ductile foams show a flat and smooth plateau [1]. In the present study, however, some strain hardening can be observed, see Fig. 8. This may be due to the relatively higher densities of the foams examined [19]. The wavy pattern in the stress–strain curve is a result of collective cell collapse and the formation of crush bands. Wavy patterns could also be generated by a brittle component in plastic yield [1]. Observation of the intermediate deformation stages can help elucidating this.

At 7% strain, the deformation is a mixture of both ductile and brittle nature in the case of S foam, since both buckling and cracking of cell walls can be discerned in Fig. 9a. Both buckling and cracking are the known deformation mechanisms of cell walls [2,20]. In Fig. 9a the crack most likely initiated at large microstructural porosities [10,11]. The crack shown in Fig. 10a supports this hypothesis. On the other hand, for the higher cooling rate foams M and H, deformation initiates in a mostly ductile manner, see Fig. 9b and 9c. Smaller microstructural porosities and finer grain size allowed buckling of the cell walls without pronounced crack generation as shown in Fig. 10b.

At a higher strain level of 25% there is no such difference in deformation behaviour: crush bands form by both buckling and cracking of cell walls as depicted in Fig. 11. Since the $\eta$ value for all types of foams is similar (Fig. 8), it is expected that during the entire deformation stage all the foams behave in a similar way. The cooling rate in the range studied here does not influence the bulk ductile–brittle nature of the foams.

## 5. Conclusions

We have demonstrated that the variation in cooling rate is a good strategy to enhance the strength of aluminium foams through modification of the macro and microstructure. Among the three cooling rates studied, the medium one produces the best result in terms of a more uniform cell size distribution and the presence of more number of smaller cells. However, a further increase in cooling rate leads to adverse effects and the structure deteriorates. The microporosity and grain size in the cell walls decreases with increasing cooling rate. The compressive strength was found to be the highest for the medium cooling rate. The study of the initial stages of deformation revealed that in foams made by slowest cooling more cracks compared to medium and highest cooling rates were generated. Cracks are believed to originate from large micropores formed during slow cooling.

## Acknowledgements

The authors would like to thank Beate Pfretzschner and Holger Kopf for their assistance in sample preparation and S. Sasidhara for his assistance with the mechanical tests.

**Reference**


[1] Gibson LJ, Ashby MF. Cellular solids – structure and properties. Cambridge: Cambridge University Press; 1999.

[2] Sugimura Y, Meyer J, He MY, Bart-Smith H, Grenstedt J, Evans AG. Acta Mater 1997;45:5245.

[3] Bart-Smith H, Bastawros AF, Mumm DR, Evans AG, Sypeck DJ, Wadley HNG. Acta Mater 1998;46:3583.

[4] Andrews E, Sanders W, Gibson LJ. Mater Sci Eng A 1999;270:113.

[5] Jeon I, Asahina T. Acta Mater 2005;53:3415.

[6] Ramamurty U, Paul A. Acta Mater 2004;52:869.

[7] Mukherjee M, Garcia-Moreno, Banhart J. Scripta Mater 2010;63:235.

[8] Matijasevic B, Banhart J. Scripta Mater 2006;54:503.

[9] Jimenez C, Garcia-Moreno F, Mukherjee M, Goerke O, Banhart J. Scripta Mater 2009;61:552.

[10] Ohgaki T, Toda H, Kobayashi M, Uesugi K, Niinomi M, Akahori T, Kobayash T, Makii K, Aruga Y. Philos Mag 2006;86:4417.

[11] Toda H, Ohgaki T, Uesugi K, Kobayashi M, Kuroda N, Kobayashi T, Niinomi M, Kuroda N, Akahori T, Makii K, Aruga Y. Met Mater Trans A 2006;37:1211.

[12] Lehmhus D, Banhart J. Mater Sci Eng A 2003;349:98.

[13] Anson JP, Gruzleski JE. Mater Charact 1999;43:319.

[14] Körner C, Arnold M, Singer RF. Mater Sci Eng A 2005;396:28.

[15] Miyoshi T, Itoh M, Akiyama S, Kitahara A. Adv Eng Mater 2000;2:179.

[16] Elmoutaouakkil A, Salvo L, Maire E, Peix G. Adv Eng Mater 2002;4:803.

[17] Paul A, Ramamurty U. Mater Sci Eng A 2000;281:1.

[18] Baumeister J, Banhart J, Weber M. Mater Des 1997;18:217.

[19] Kolluri M, Karthikeyan S, Ramamurty U. Met Mater Trans A 2007;38:2006.

[20] Kolluri M, Mukherjee M, Garcia-Moreno F, Banhart J, Ramamurty U. Acta Mater 2008;56:1114.

[21] Mukherjee M, Kolluri M, Garcia-Moreno F, Banhart J, Ramamurty U. Scripta Mater 2009;61:752.

[22] Bastawros AF, Bart-Smith H, Evans AG. J Mech Phys Solids 2000;48:301.

[23] Garcia-Moreno F, Raffaele N, Banhart J. In: Stephani G, Kieback B, editors. Cellular metals for structural and functional applications (CellMet), Dresden, 2009. p.133.

[24] Gergely V, Clyne TW. Acta Mater 2004;52:3047.

[25] Brunke O, Hamann A, Cox SJ, Odenbach S. J Phys Condens Matter 2005;17:6353.

[26] Körner C, Berger F, Arnold M, Stadelmann C, Singer RF. Mater Sci Tech 2000;16:781.

[27] Stanzick H, Wichmann M, Weise J, Helfen L, Baumbach T, Banhart J. Adv Eng Mater 2002;4:814.

[28] Shabestari SG, Malekan M. Can Met Quarterly 2005;44:305.

[29] Khan S, Ourdjini A, Hamed QS, Alam Najafabadi MA, Elliott R. J Mater Sci 1993;28:5957.

[30] Escobar de Obaldia E, Felicelli SD. J Mater Process Tech 2007;191:265.

[31] Andrews EW, Gioux G, Onck P, Gibson LJ. Int J Mech Sci 2001;43:701.

[32] Ashby MF, Evans AG, Fleck NA, Gibson LJ, Hutchinson JW, Wadley HNG. Metal foams – a design guide. Boston: Butterworth-Heinemann; 2000.

[33] Amsterdam E, De Hosson JThM., Onck PR. Acta Mater 2006;54:4465.

[34] Mukherjee M, Garcia-Moreno F, Banhart J, Kolluri M, Ramamurty U. In: Lefebvre LP, Banhart J, Dunand D, editors. Porous metals and metallic foams, Pennsylvania: DEStech Publications, 2008. p.347.

[35] Sugimura Y, Rabiei A, Evans AG, Harte AM, Fleck NA. Mater Sci Eng A 1999;269:38.

[36] Dannemann KA, Lankford Jr J. Mater Sci Eng A 2000;293:157.

**Figure captions**

Fig. 1. Schematic of the experimental set-up used for producing foams.

Fig. 2. Orientation of the six sections inside the sample, starting at 5 mm from the outer surface and with intervals of 5 mm.

Fig. 3. Microstructure of cell walls of the foams cooled with different rates (a) and (b) S; (c) and (d) M; and (e) and (f) H. Arrows indicate shrinkage porosity.

Fig. 4. Microstructure of S foam. Arrow indicates shrinkage porosity that is in contact with the main pore.

Fig. 5. 2D cell size distribution for (a) S, (b) M and (c) H foams. The distributions are fitted with log-normal functions (solid lines).

Fig. 6. 2D cell size distribution for (a) S, (b) M and (c) H foams. The distributions are fitted with log-normal functions (solid lines).

Fig. 7. Circularity vs. equivalent diameter of the cells in the (a) S, (b) M, and (c) H foams. The broken line at 3.18 mm defines the boundary between small and large cells, see text.

Fig. 8. Compressive stress and energy absorption efficiency of S, M and H foams vs. strain. Relative densities are 20.88%, 24.84% and 24.29% for S, M and H foams, respectively. Strategies employed to extract the compressive strength, $\sigma_p$, and the densification strain, $\varepsilon_d$, are also shown.

Fig. 9. X-ray tomographic reconstruction (3D image) of foams after 7% strain – (a) S, (b) M, and (c) H. Loading axis is from the top to bottom of the image. Ellipses indicate some of the deformed cell walls. The arrow in (a) shows a crack. The microstructure of the region in (a) marked by a square is shown in Fig. 10a.

Fig. 10. Microstructure of cell walls of foams after 7% total strain – (a) S, (b) H. A pre-existing cell wall porosity is indicated by white solid lines, the broken lines connect the separated ends of that porosity.

Fig. 11. X-ray tomographic reconstruction (3D image) of foams after 25% strain –(a) S and (b) H. Loading axis is from the top to bottom of the image. Ovals indicate crush bands.

Fig. 12. Comparison of the macrostructures of a M (a, b) and a H (c, d) foam with similar density. (a,c) X-ray tomographic reconstructions; (b,d) cell size distributions. The tomograms represent central sections perpendicular to each other and the loading direction is from the top to bottom of the images. $D_{mean}$ in each case was determined from log-normal fitting (solid line in c and d).

Table 1

The number of samples used for different analysis. X-ray tomography and density were performed on each sample (except the ones used for microstructure analysis) before compression testing

| Cooling rate (K/s) | Number of samples | | | | | |
|---|---|---|---|---|---|---|
| | Total | Microstructure | Tomography (structure) and density | Strain 70% | Strain 7%* | Strain 25% |
| 0.9 ± 0.1 (S) | 7 | 1 | 6 | 4 | 1 | 1 |
| 2.5 ± 0.1 (M) | 6 | 1 | 5 | 4 | 1 | – |
| 3.5 ± 0.2 (H) | 7 | 1 | 6 | 4 | 1 | 1 |

* microstructures of these samples were also analyzed after deformation

Table 2

Analysis of the cell size and circularity. $R^2$ represents the quality of a fit of the cell size distribution with a log-normal function.

| Sample | $D_{mean}$ (mm) | | | | | Circularity (Arithmetic mean) |
|---|---|---|---|---|---|---|
| | Arithmetic mean | Based on the number of cells (Fig. 5) | $R^2$ | Based on the area fraction of cells (Fig. 6) | $R^2$ | |
| S | 1.47 ± 1.04 | 1.26 ± 0.72 | 0.95 | 2.26 ± 0.46 | 0.91 | 0.76 ± 0.13 |
| M | 1.38 ± 0.94 | 1.16 ± 0.69 | 0.96 | 2.27 ± 0.53 | 0.95 | 0.78 ± 0.12 |
| H | 1.40 ± 1.00 | 1.17 ± 0.69 | 0.98 | 2.36 ± 0.57 | 0.90 | 0.77 ± 0.13 |

Table 3

Area and number fraction of large cells defined as those cells for which $D_{large\text{-}cell} > D_{mean} + 2\mu$ holds, where $\mu$ is the standard deviation

| Sample | $D$ > 3.18 mm | |
|---|---|---|
| | Area fraction, % | Number fraction, % |
| S | 38.1 | 5.6 |
| M | 32.2 | 4.5 |
| H | 37.3 | 5.2 |

Table 4

Relative density, compressive strength and energy absorption of three types of samples.

Numbers in bracket indicate the number of samples that were used to acquire that data

| Sample | Relative density, $\rho^*\times100$ (%) | Compressive strength, $\sigma_p$ (MPa) | Normalised $\sigma_p$ $(\sigma_p/(\rho^*)^n)$ (MPa) | | Energy absorption $W$ ($MJ/m^3$) |
|---|---|---|---|---|---|
| | | | $n$ =1.5 | $n$ = 2 | |
| S | 21.1 ± 3% (6) | 11.9 ± 10% (6) | 123 ± 14% | 267 ± 13% | 8.78 ± 11% (4) |
| M | 24.1 ± 4% (5) | 16.7 ± 8% (5) | 141 ± 9% | 287 ± 8% | 12.21 ± 9% (4) |
| H | 23.5 ± 4% (6) | 14.8 ± 8% (6) | 130 ± 5% | 267 ± 3% | 11.26 ± 10% (4) |

**Figure 1**

Click here to download high resolution image

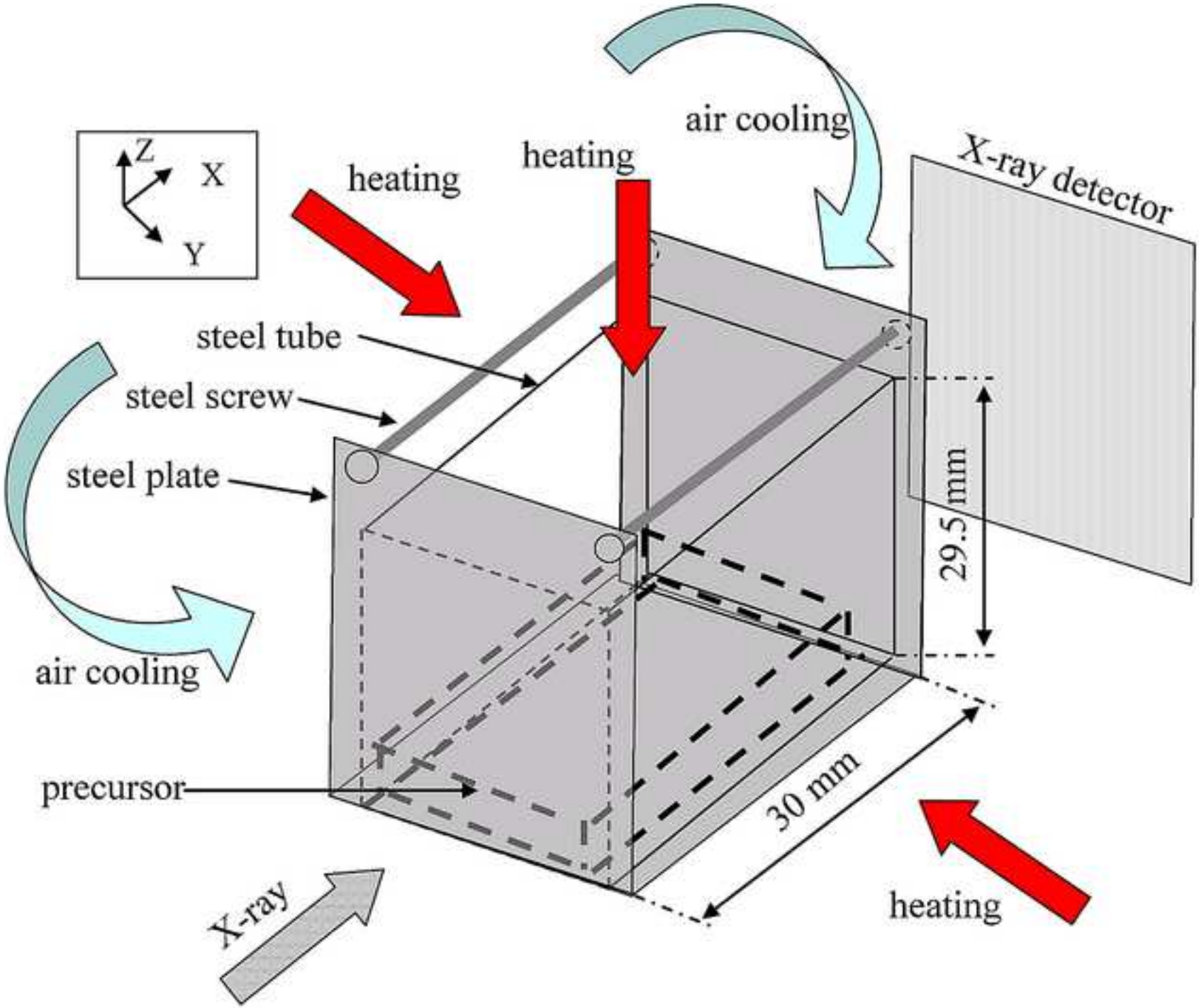

Figure 2
Click here to download high resolution image

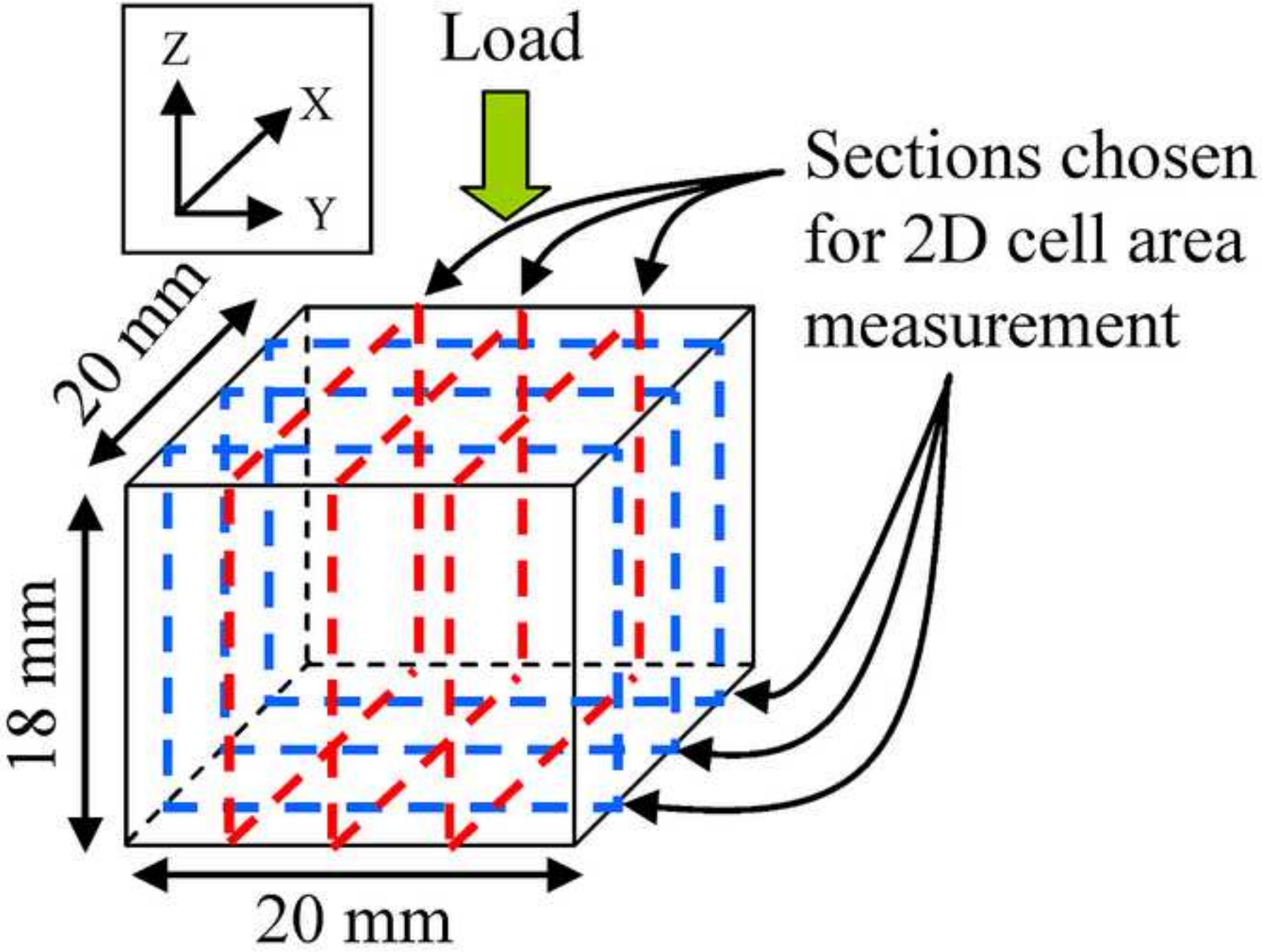

**Figure 3a and 3b**

**Click here to download high resolution image**

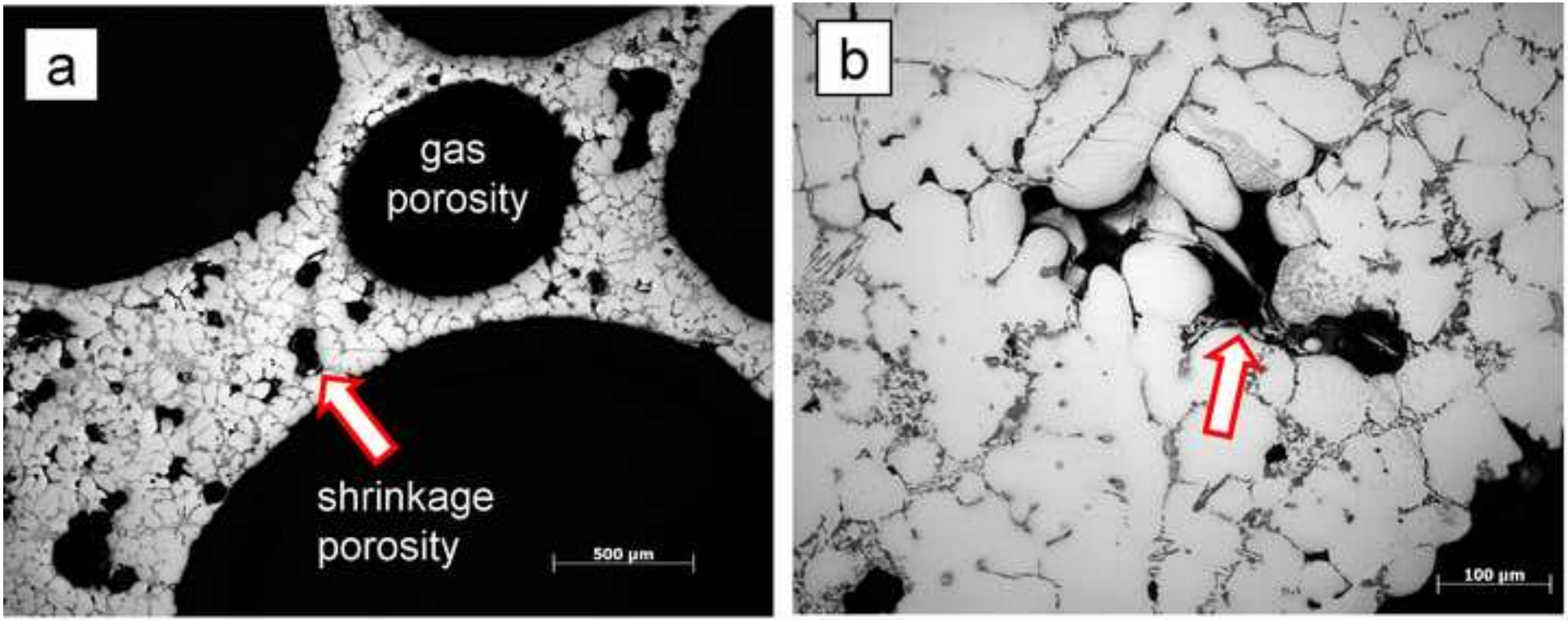

**Figure 3c and 3d**

**Click here to download high resolution image**

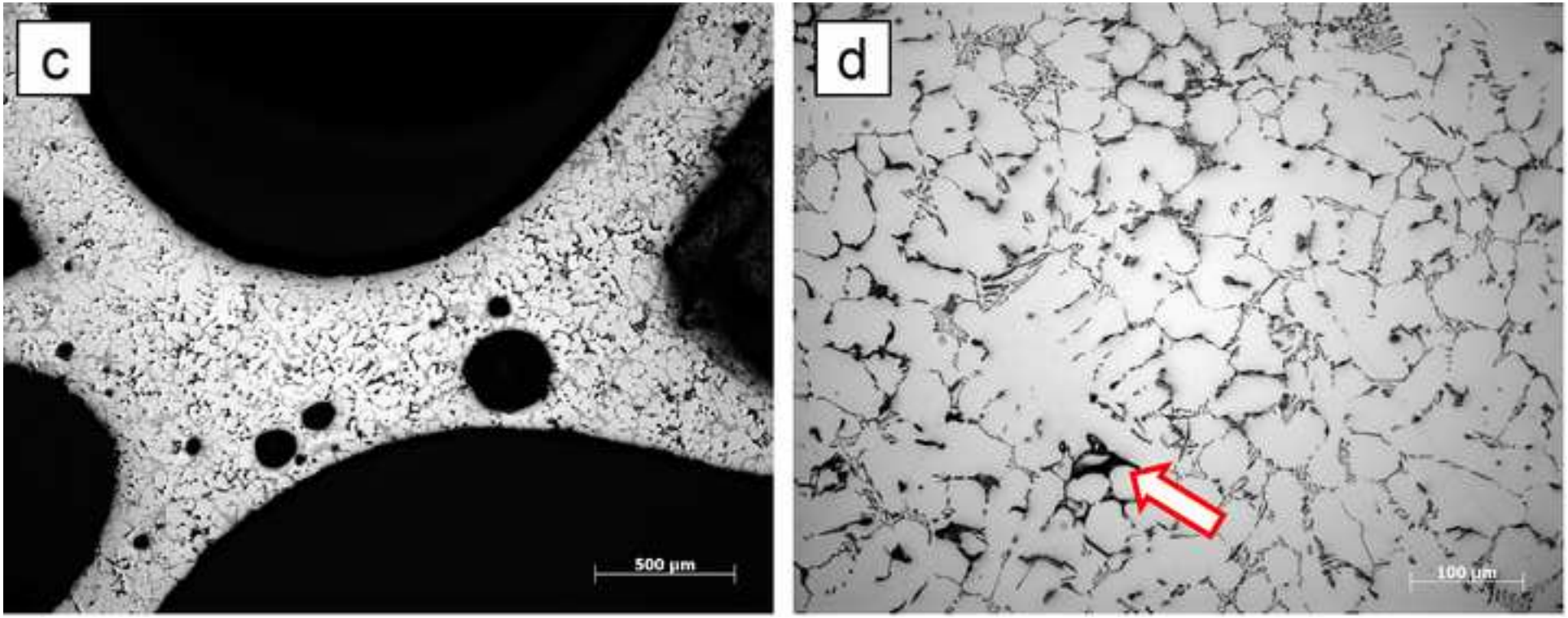

**Figure 3e and 3f**

**Click here to download high resolution image**

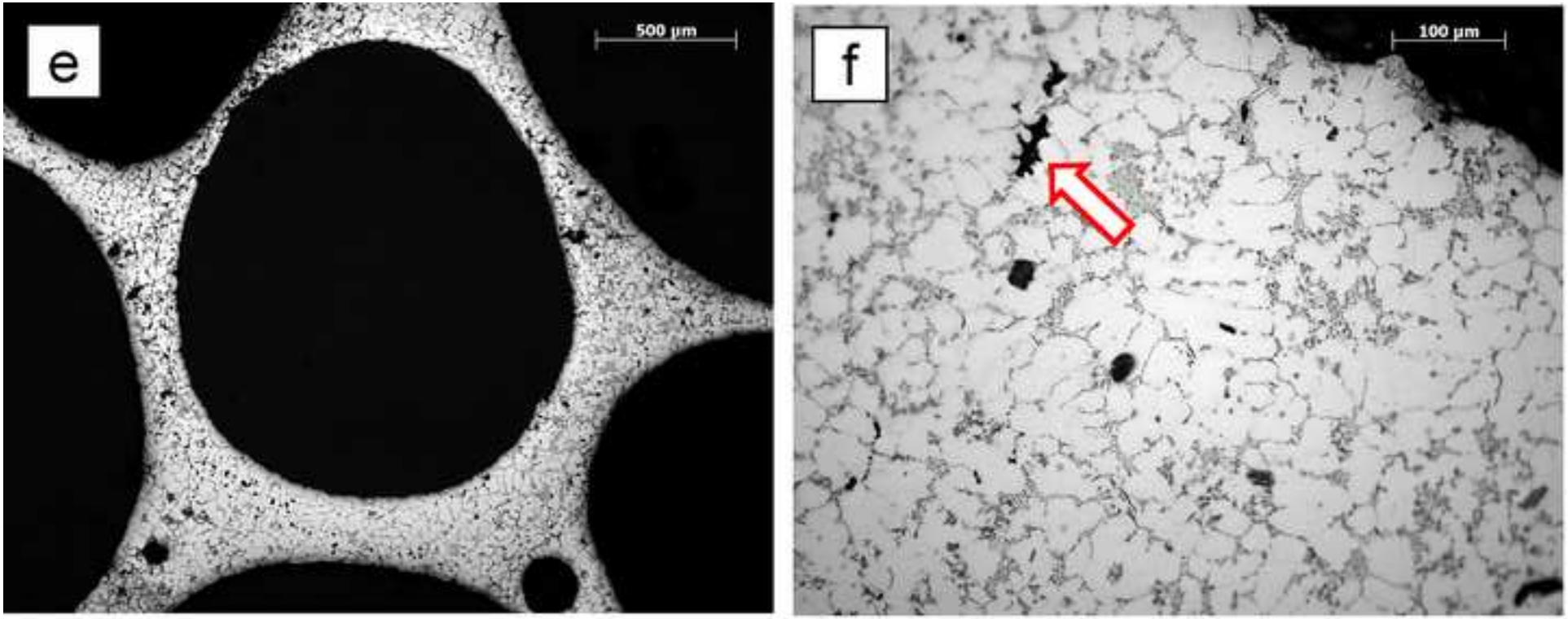

**Figure 4**

Click here to download high resolution image

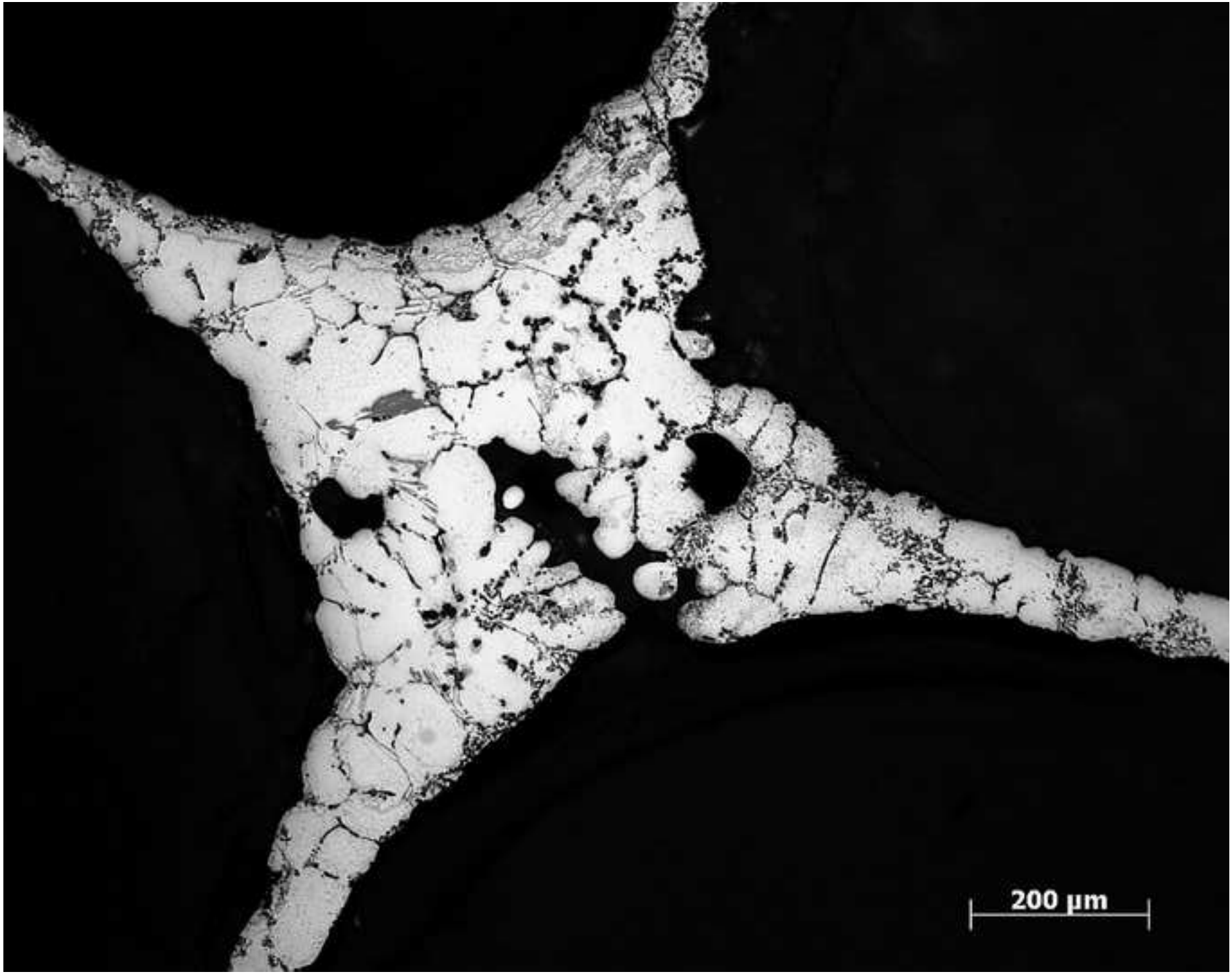

Figure 5a

Click here to download high resolution image

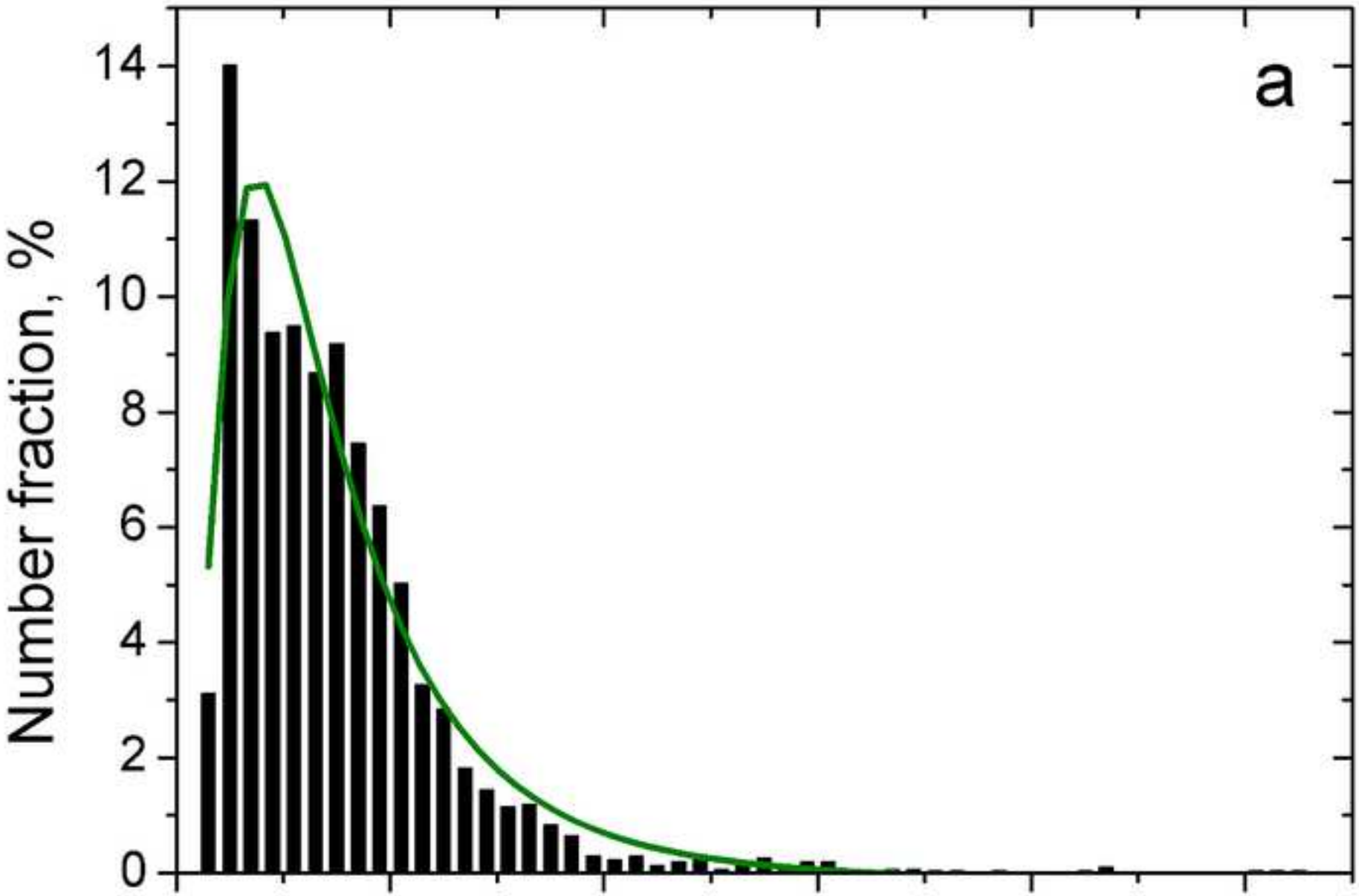

Figure 5b

Click here to download high resolution image

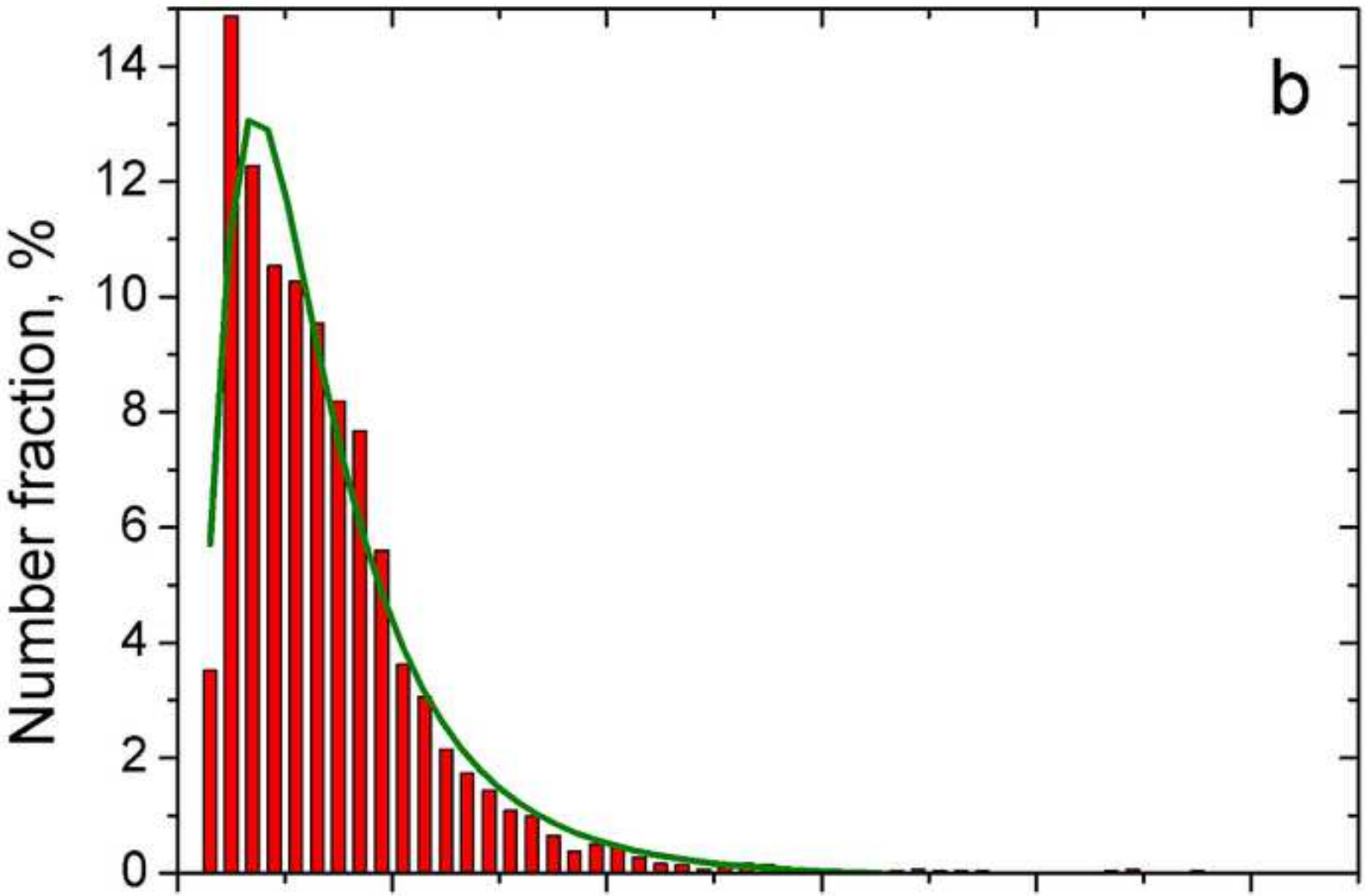

Figure 5c

Click here to download high resolution image

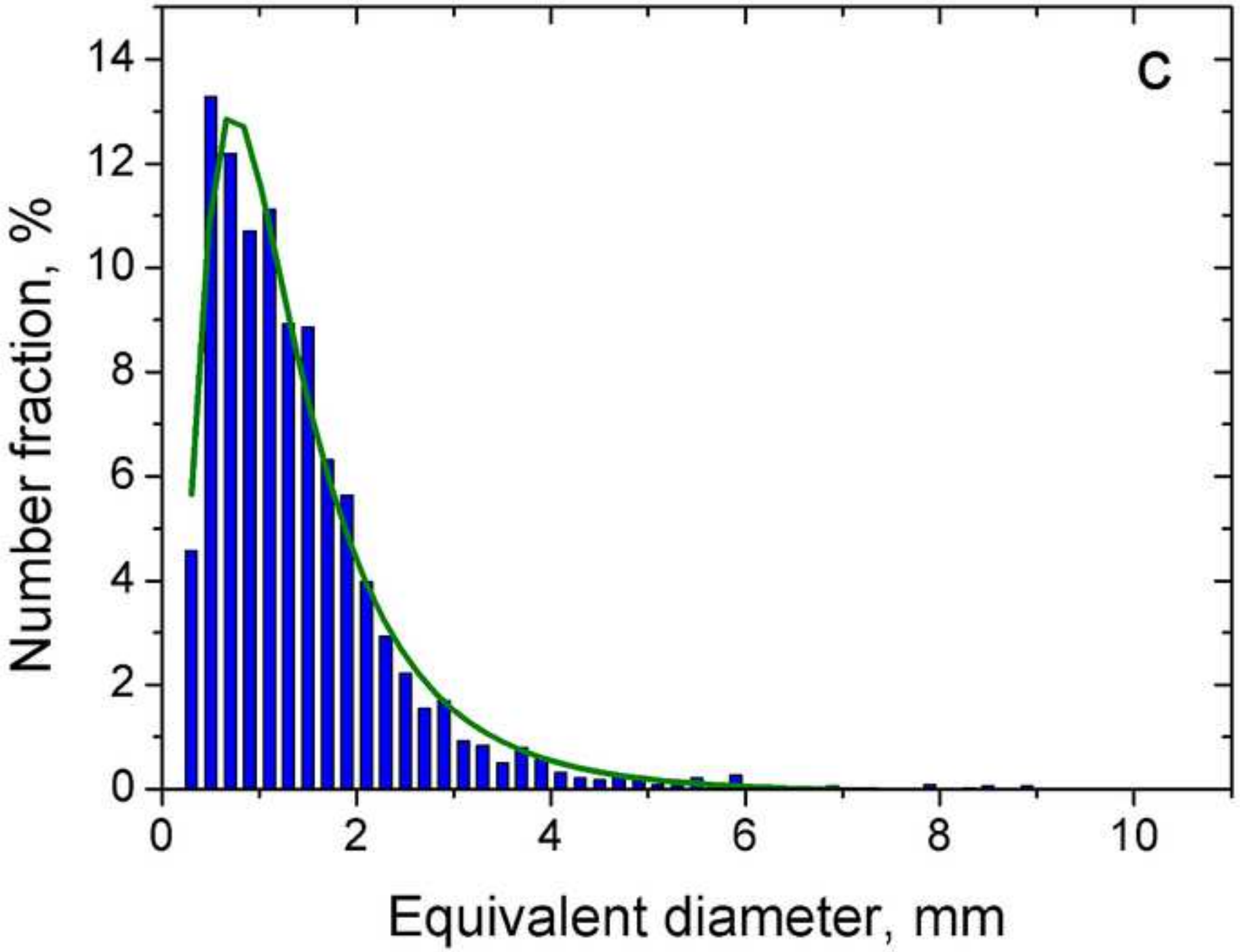

Figure 6a

Click here to download high resolution image

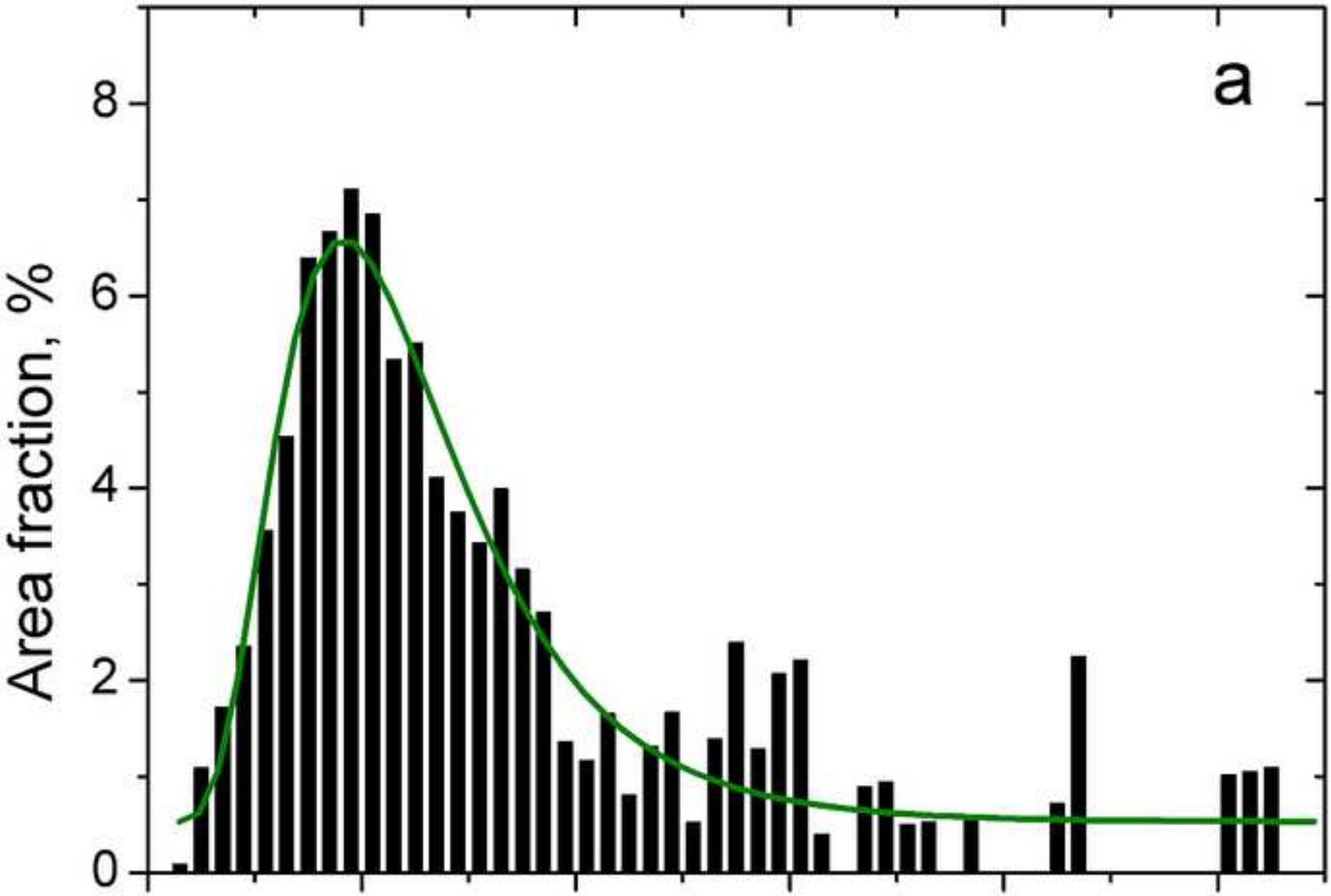

Figure 6b

Click here to download high resolution image

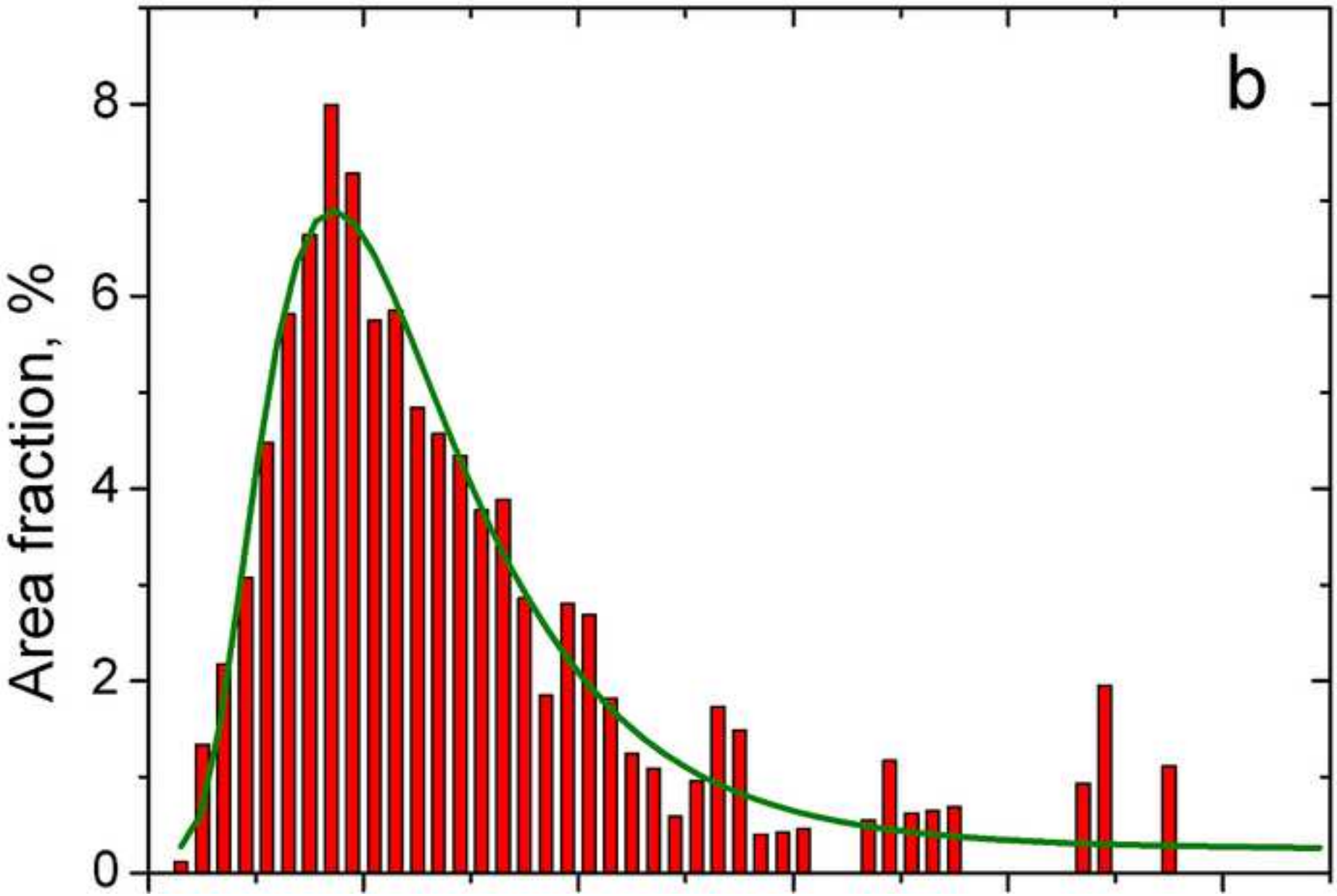

Figure 6c
Click here to download high resolution image

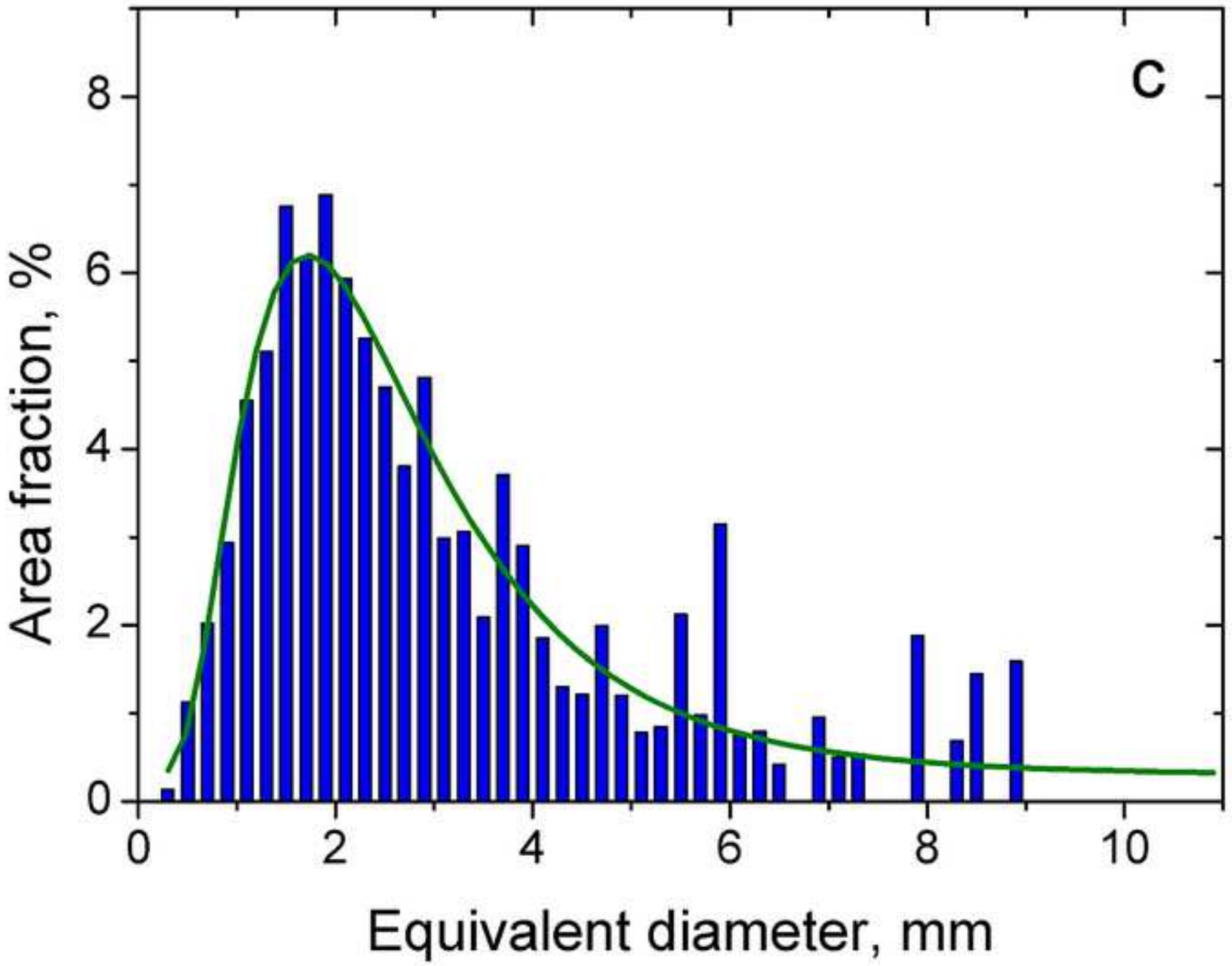

Figure 7a

Click here to download high resolution image

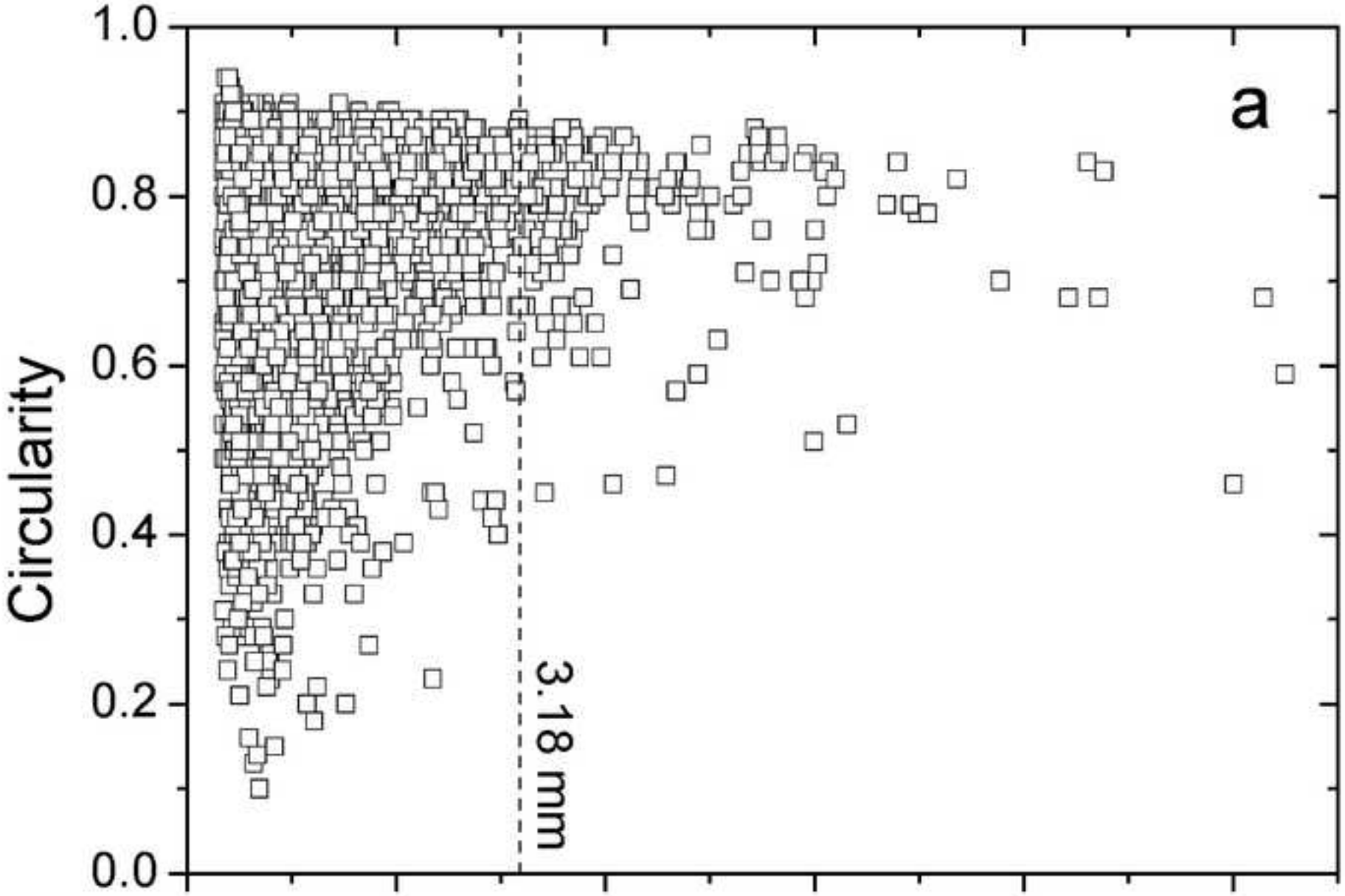

Figure 7b

Click here to download high resolution image

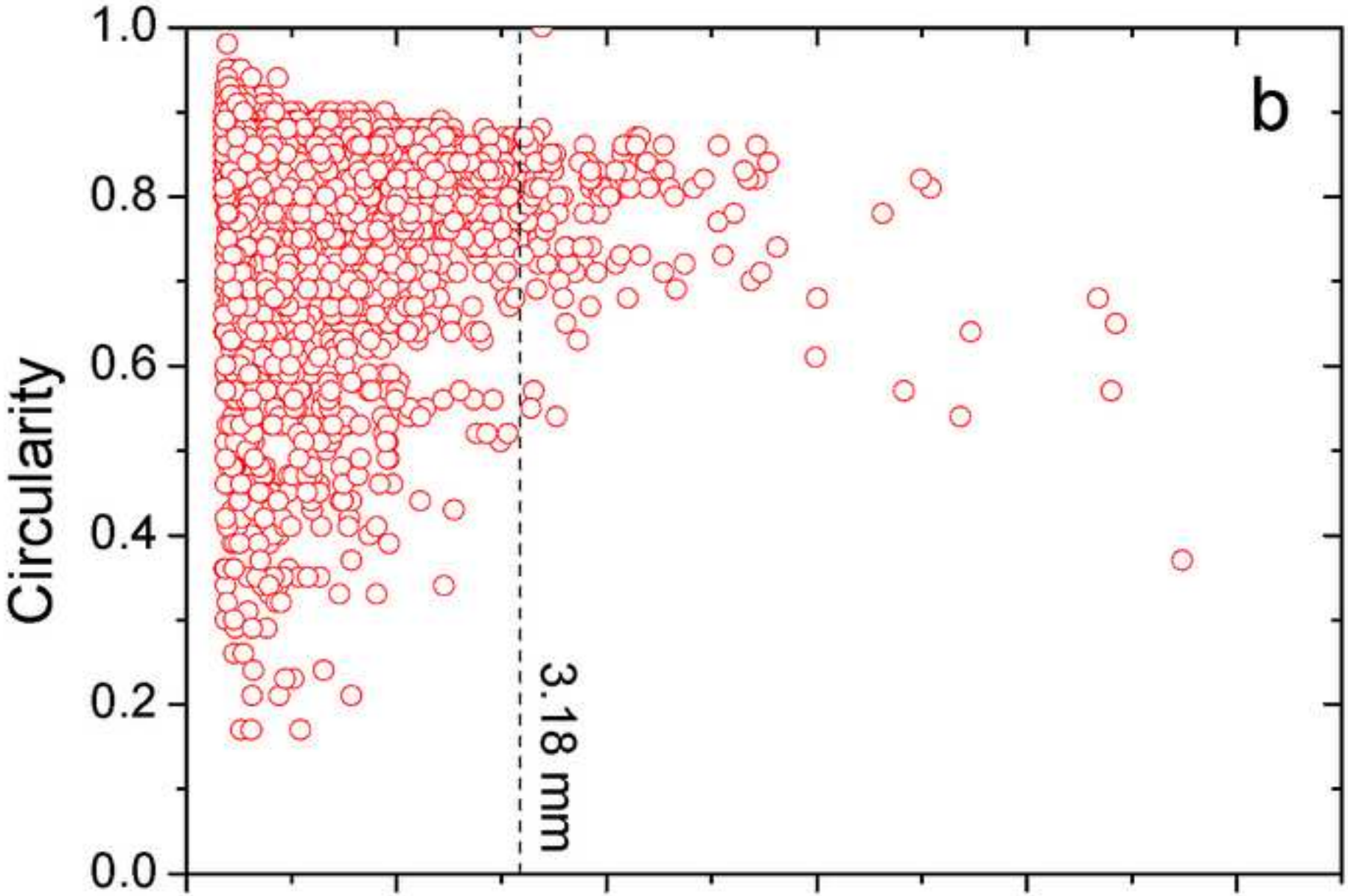

Figure 7c
Click here to download high resolution image

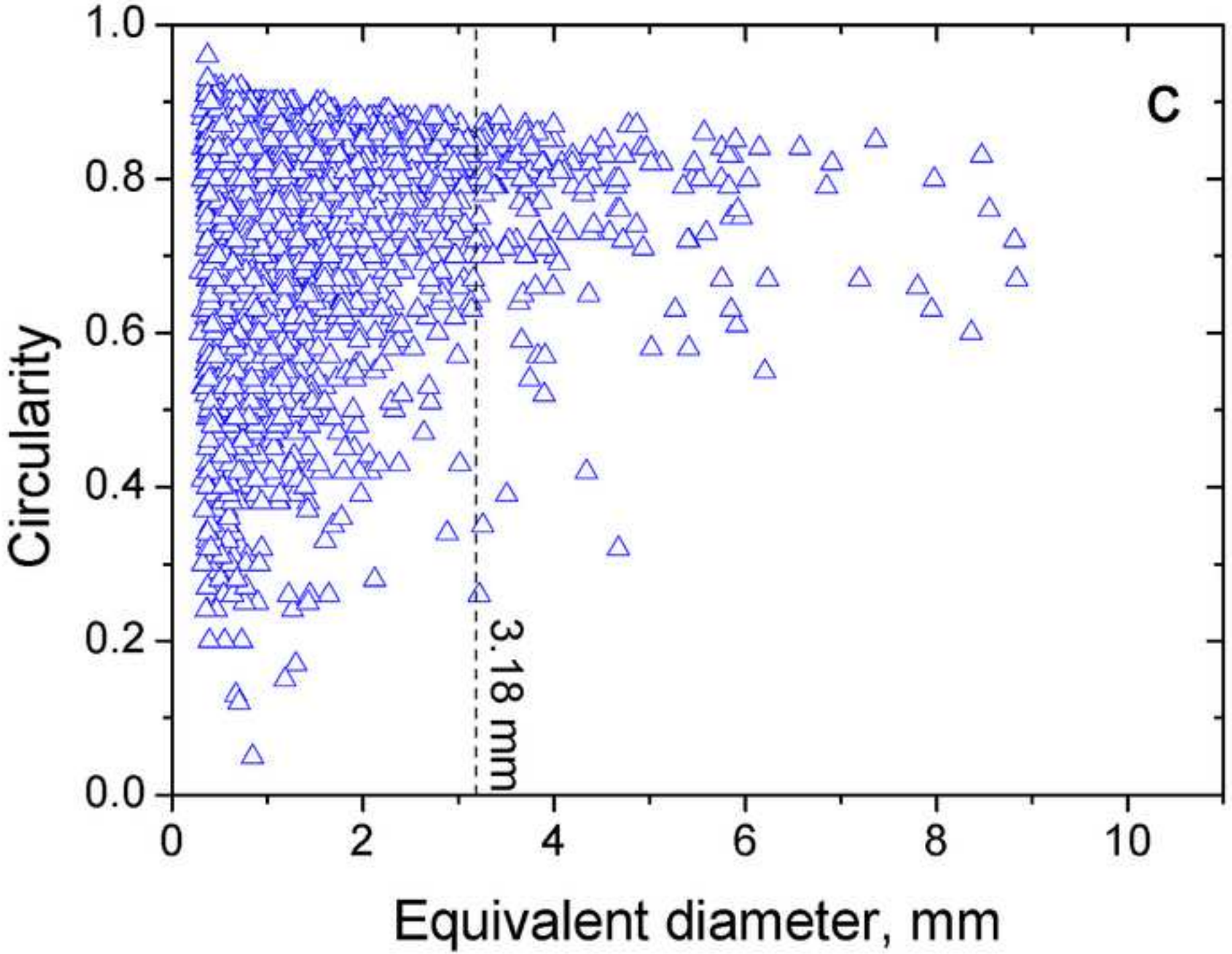

Figure 8

Click here to download high resolution image

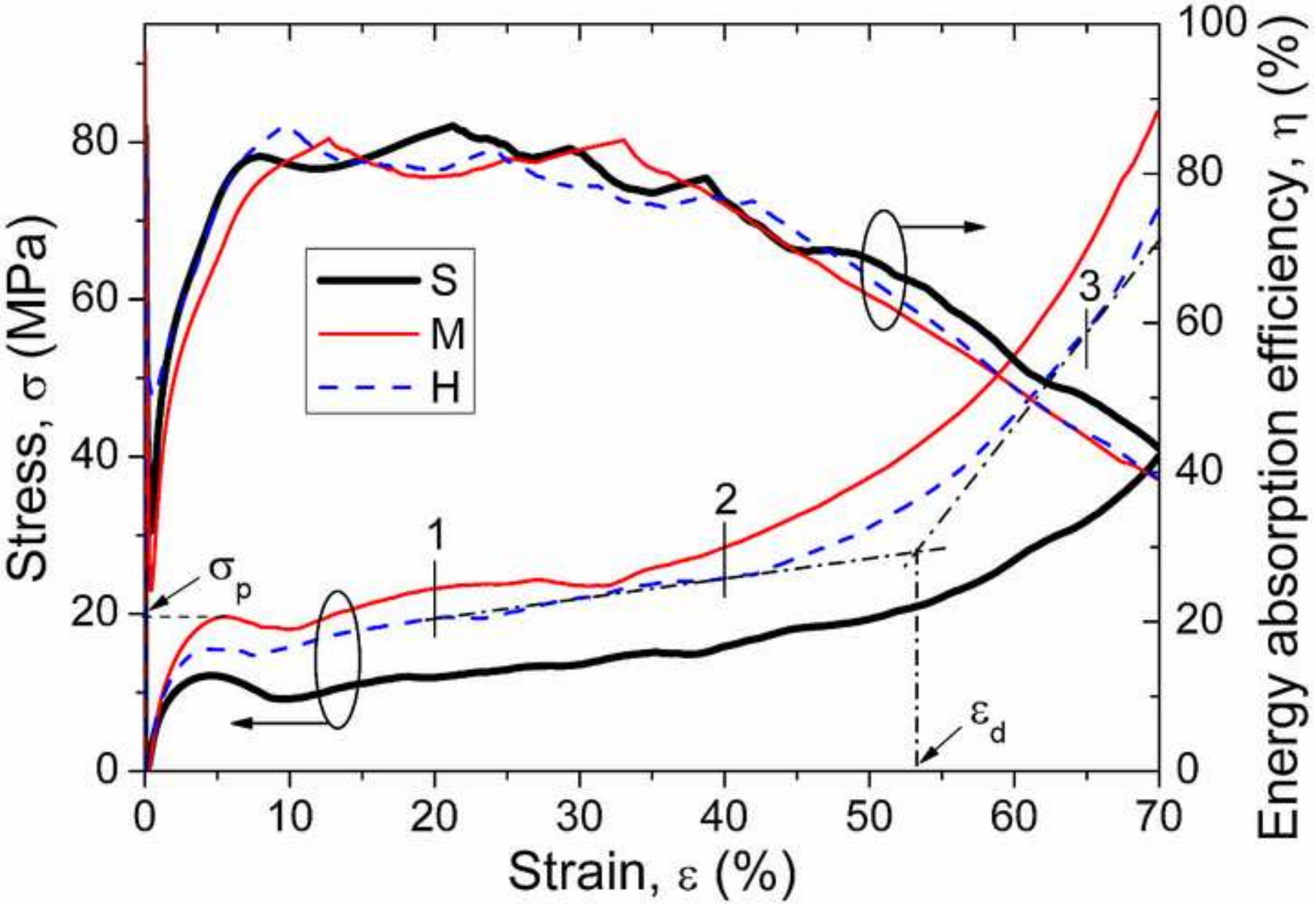

**Figure 9-a-b-c**

Click here to download high resolution image

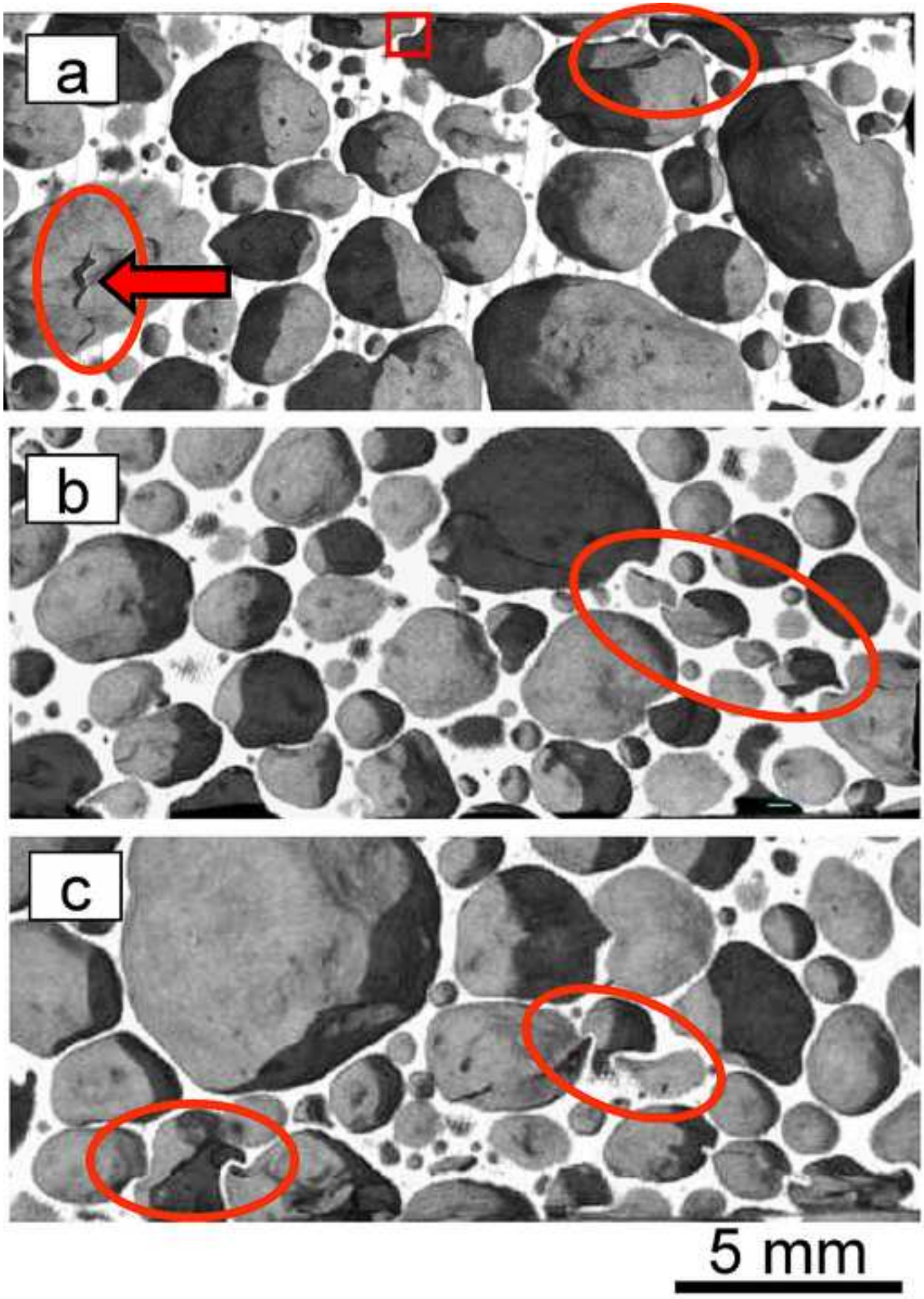

**Figure 10-a-b**

Click here to download high resolution image

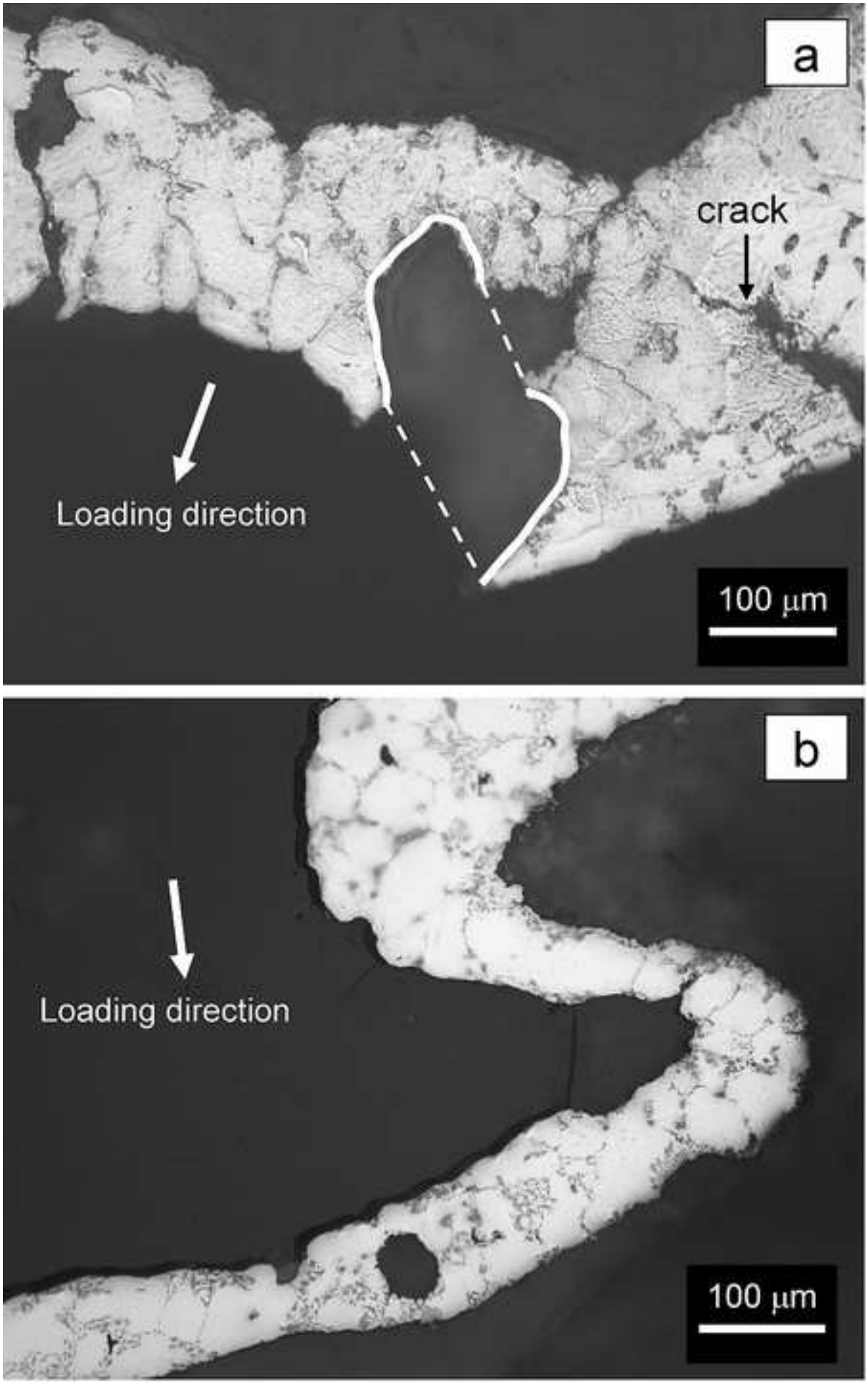

Figure 11-a-b

Click here to download high resolution image

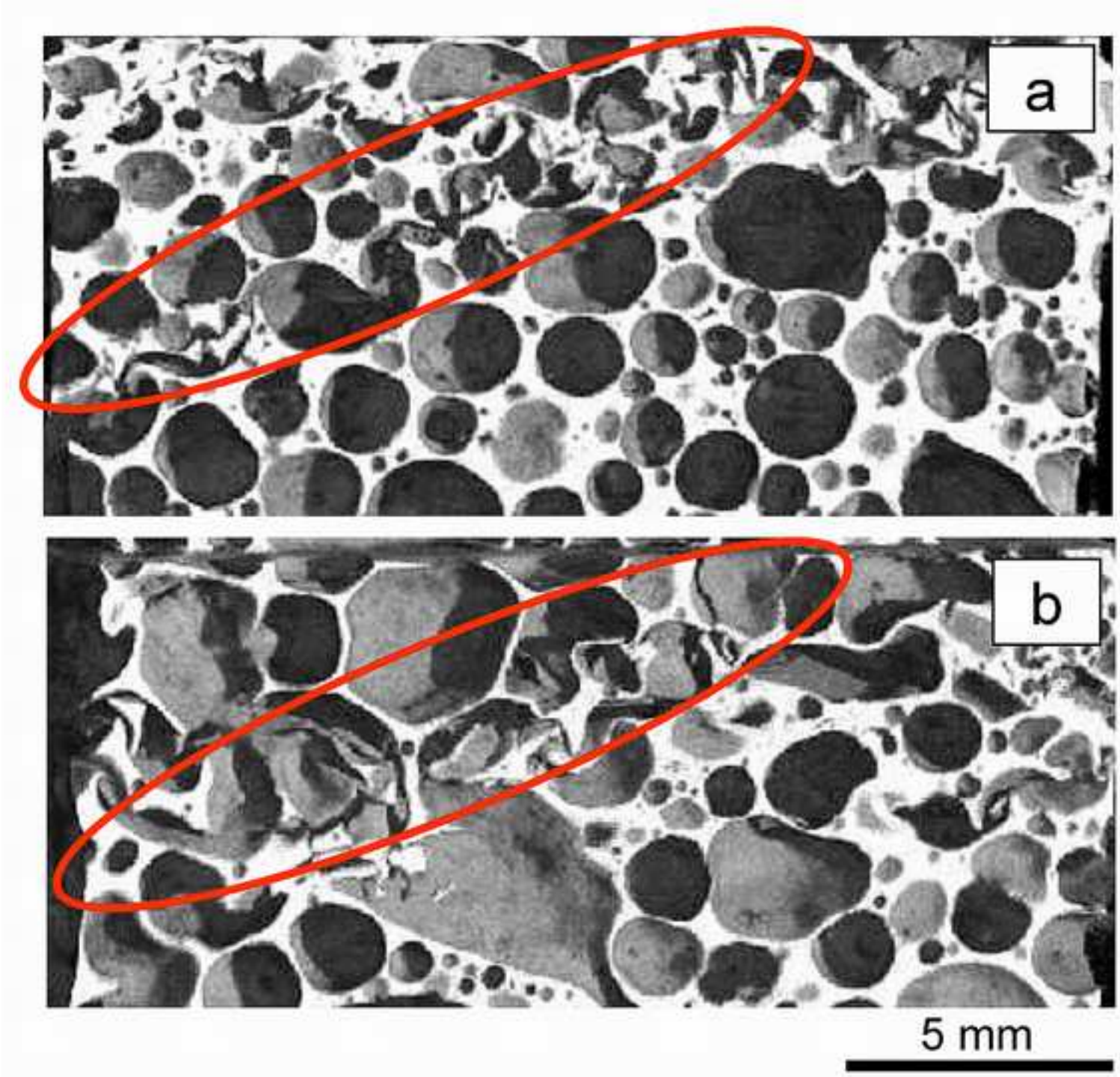

Figure 12a
Click here to download high resolution image

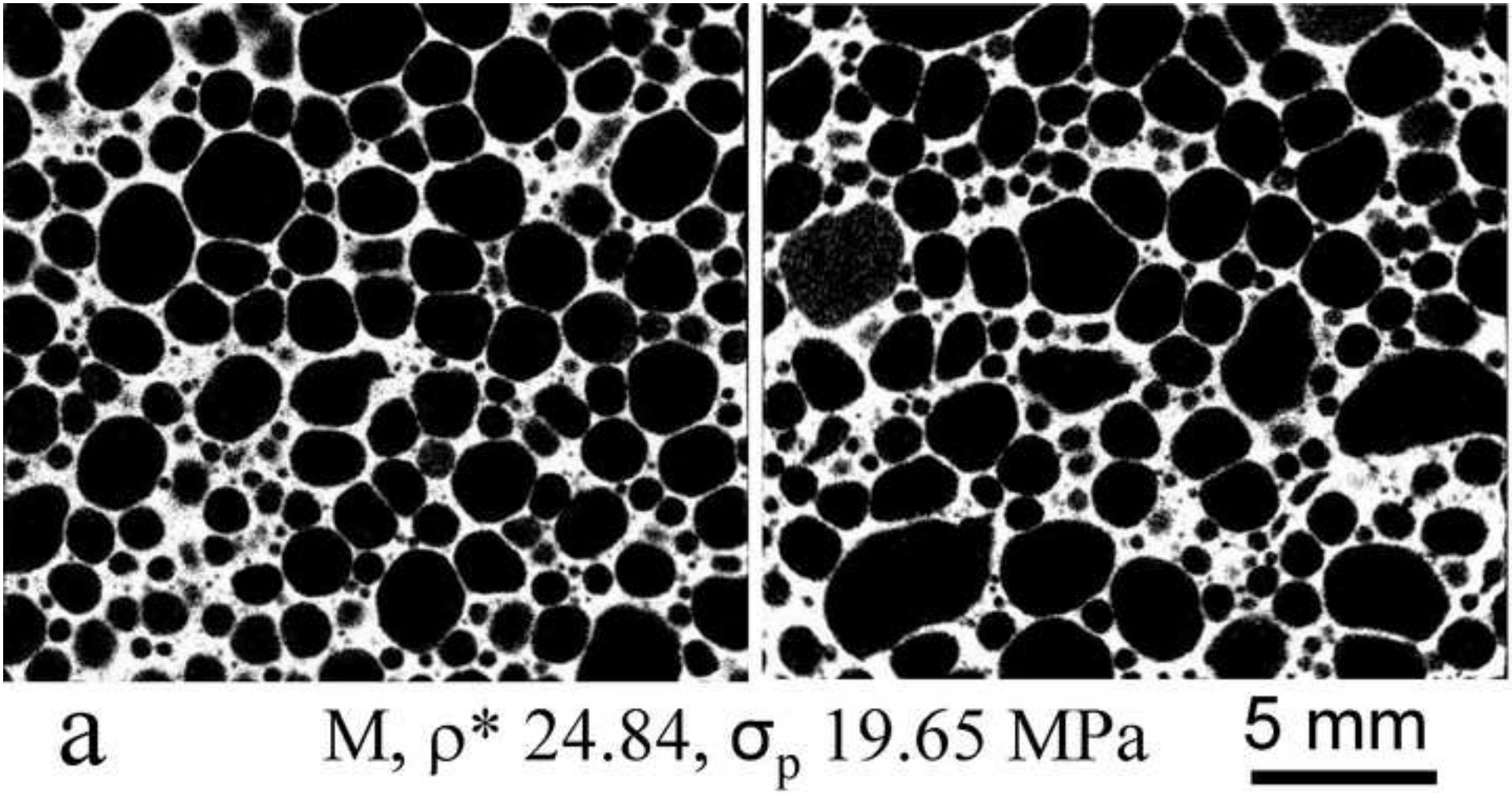

Figure 12b
Click here to download high resolution image

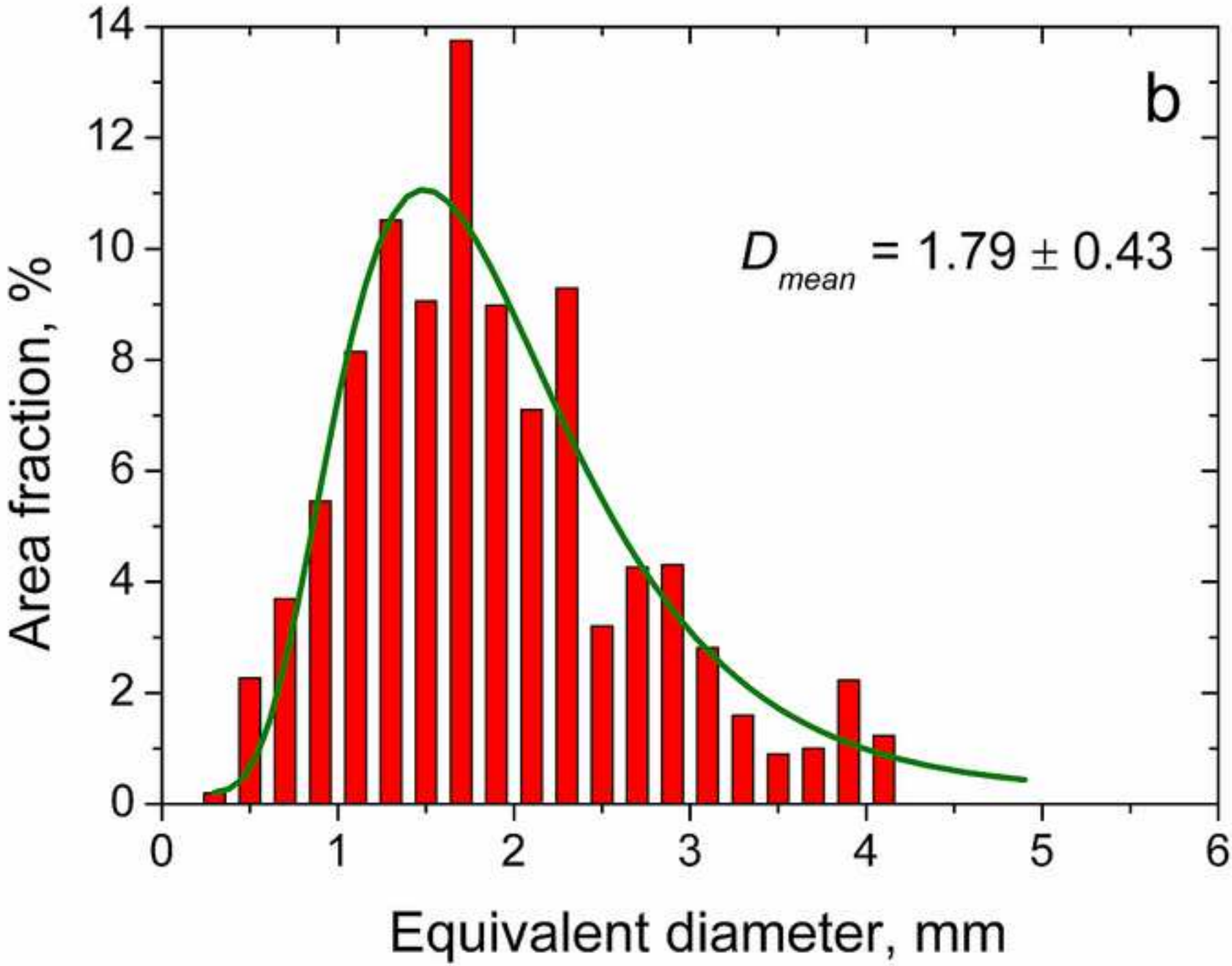

Figure 12c
Click here to download high resolution image

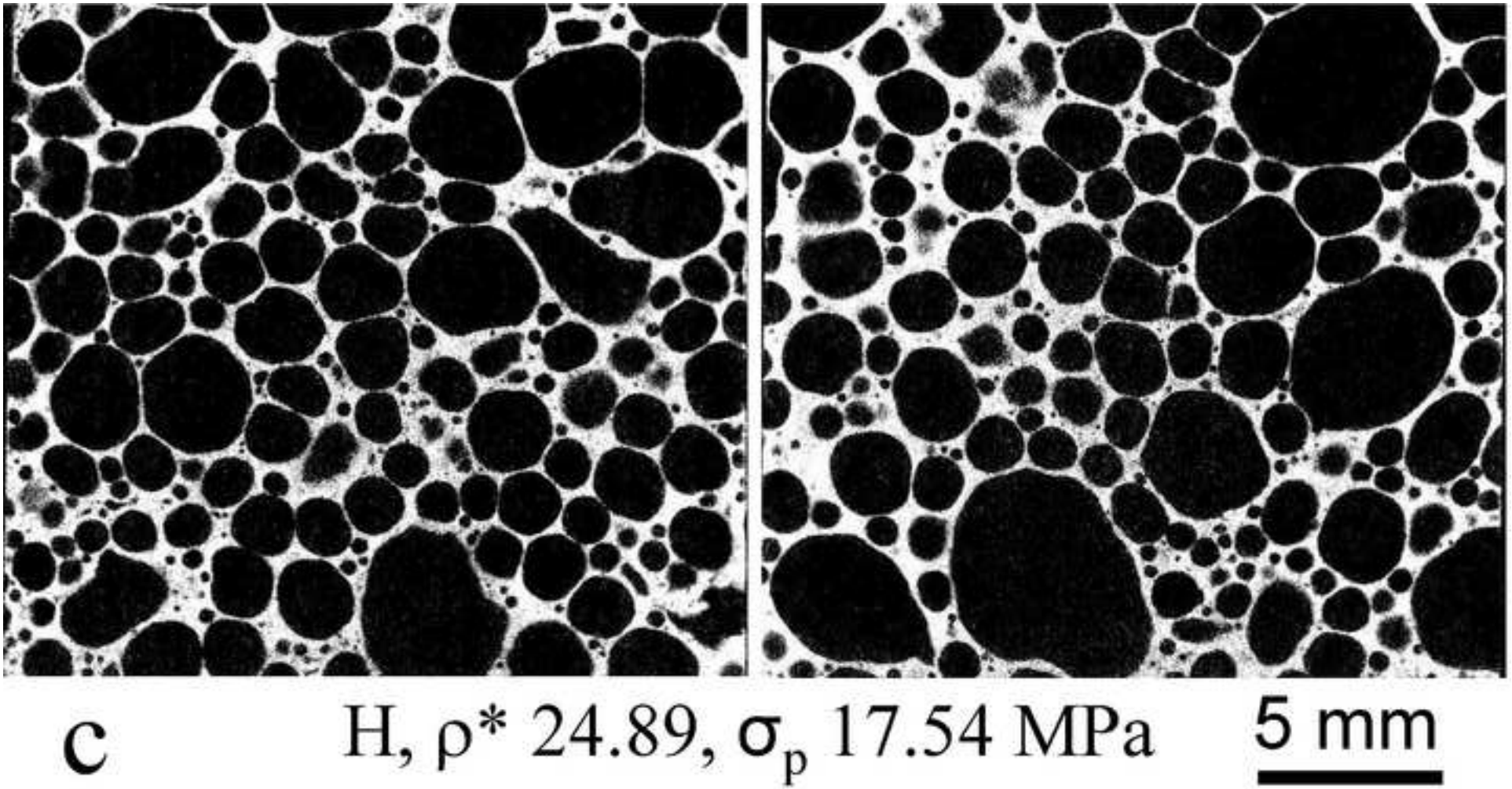

Figure 12d

Click here to download high resolution image